Title
The Impact of the Central Asian Mountains on Downstream Storminess and Monsoon Onset

Author
Park, Hyo Seok

Publication Date
2010

Peer reviewed|Thesis/dissertation

The Impact of the Central Asian Mountains on Downstream Storminess and Monsoon Onset

by

Hyo Seok Park

A dissertation submitted in partial satisfaction of the
requirements for the degree of
Doctor of Philosophy

in

Geography

in the

Graduate Division

of the

University of California, Berkeley

Committee in charge:
Professor John C.H. Chiang, Chair
Professor Kurt M. Cuffey
Professor Inez Y. Fung

Spring 2010

The Impact of the Central Asian Mountains on Downstream Storminess and Monsoon Onset

by

Hyo Seok Park

Abstract

The Impact of the Central Asian Mountains on Downstream Storminess and Monsoon Onset

by

Hyo Seok Park

Doctor of Philosophy in Geography
University of California, Berkeley
Professor John Chiang, Chair

In the first part of the thesis, the role of the Central Asian mountains on North Pacific storminess is examined using an atmospheric general circulation model by varying the height and area of the mountains. A series of model integrations shows that the presence of the Central Asian mountains suppresses North Pacific storminess by 20-30% during boreal winter. Their impact on storminess is found to be small during other seasons. Two main causes of the reduced storminess are diagnosed. First, the decrease in storminess appears to be associated with a weakening of downstream eddy development. The mountains disorganize the zonal coherency of wave packets and refract them more equatorward. As the zonal traveling distance of wave packets gets substantially shorter, downstream eddy development gets weaker, leading to the weakening of transient eddy kinetic energy and storminess. Second, the Central Asian mountains suppress the global baroclinic energy conversion. The decreased baroclinic energy conversion, particularly over the Eastern Eurasian continent decreases the number of eddy disturbances entering into the Western North Pacific. The 'barotropic governor' does not appear to be a dominant factor in explaining the results.

In the second part of the thesis, the impact of the Tibetan Plateau on the onset of the South Asian summer monsoon is examined using an atmospheric general circulation model. A series of model integrations shows that rainfall increases downstream of the mountains, whereas upstream of the mountains experiences anomalous subsidence. In particular, the Tibetan Plateau triggers low-level cross-equatorial flow and substantial rainfall over the Bay of Bengal during the pre-monsoon season (April-May). While the low-level cross-equatorial flow begins in May, the monsoon's onset over the Arabian Sea is suppressed until early June. The delayed onset over the Arabian Sea is probably because of the anomalous subsidence induced by the earlier moist convection over the Bay of Bengal. It is suggested that the earlier rainfall over the Bay of Bengal could be the response of stationary waves to the orographic forcing, such as low-level cyclonic motions downstream of the Tibetan Plateau. Because low-level westerlies exist over the Southern Tibetan Plateau during pre-monsoon season, the stationary wave response to the mountains is likely to occur.

To my grandma
who wished my success..

Table of Contents

List of Figures

List of Tables

Acknowledgements

I would like to thank my thesis advisor, John Chiang, for having me study and work independently in Berkeley, a beautiful sunny city. While I was allowed to work independently, I could not have written this thesis without guidance and support of John Chiang. I greatly appreciate his willingness to start me off on a path, let me wander independently, and help me finding out meaningful physics out of many random ideas.

Conversations with Inez Fung, one of my thesis committee, were invaluable. To be honest, the quality of my thesis was significantly improved while I was trying to answer some questions raised by Inez during my presentation. I also would like to thank Kurt Cuffy for his encouraging words. It was exciting to attend his Glaciology class and interact with him. The thesis is also benefited from numerous interactions with Ben Lintner and Seok-Woo Son. I really enjoyed working with them.

I would like to thank my colleagues at Berkeley. I particularly wish to thank Andrew Friedman who has always been willing to correct my disastrous grammar errors. He may have spent more than 100 hours in proofing my writing during the past five years. I also would like to thank Ching-Yee Chang and Shih-Yu Lee, both of whom have always been passionate in discussing climate dynamics with me. Shih-Yu encouraged me when I was having tough time. Many Berkeley people not named individually here were an important part of my graduate course, including my roommates, administrative staff and fellow students.

My special thanks go to my parents. I would not have finished graduate school without their financial support for hiring full-time babysitters. I should acknowledge babysitters who took care of my daughter, Jiwon for the past two years – they really loved Jiwon. I feel an obligation that I should compensate their over-working fees sometime in the future. Finally, I would like to thank my wife Eun Young, who took care of Jiwon for the past two years and patiently waited the completion of my degree.

Chapter 1: Introduction

Zonally asymmetric atmospheric circulations in response to major mountains are one of the most marvelous features characterizing the Earth's atmosphere. In a barotropic atmosphere, where isobaric surfaces coincide with isopycnal surfaces, analytical approaches are possible using a beta-plane approximation and Potential Vorticity (PV) conservation. Of course dampings have to be represented in simplified forms – Ekman damping mimicking the boundary layer drag is a good example. Based on these simplifications, stationary wave theory has been quite successful in explaining the global-scale, zonally-asymmetric flows in mid-latitudes. The most well-known application is the topographic Rossby wave model by Charney and Eliassen (1949) based on the quasi-geostrophic framework. The simple quasi-geostrophic model of Charney and Eliassen (1949) explains the longitudinal distribution of mid-latitude 500 hPa geopotential heights during the boreal winter surprisingly well.

Even though the simple model appears successful in explaining the global-scale zonal asymmetries in mid-latitudes, it is unlikely that the simple model can be applied to smaller-scale motions. Experiments using a comprehensive Atmospheric General Circulation Model (AGCM) suggest that the notoriously low sea-level pressure over the arctic Atlantic Ocean, which was named as the 'Icelandic lows', is well simulated without the major mountains (Held 1985). Furthermore, Held (1985) suspects that the surprising performance of the simple model by Charney and Eliassen (1949) could be coincident, considering that the zonally-asymmetric diabatic heating field can explain a major portion of the northern winter stationary waves.

Latent heating as an essential ingredient for stationary waves: The interaction between latent heating and large-scale atmospheric circulations is arguably one of the least-understood dynamics in the Earth's atmosphere. Major mountains are known to substantially perturb the diabatic heating field, which would in turn affect the atmospheric circulations via nonlinear interactions with the topography (Ting 1994; Rodwell and Hoskins 1996; 2001; Held et al. 2002). In particular, the linear response of stationary waves to the Tibetan Plateau is locally limited, whereas the full nonlinear response – including the interactions between the altered diabatic heating field and the Tibetan Plateau – occurs globally (Held et al. 2002). These experiments by Held et al. (2002) highlight the importance of latent heating as an essential ingredient for amplifying the topography-forced stationary waves.

In the low-latitudes, the response of diabatic heating field to the mountains, such as the Tibetan Plateau, is likely to be a lot stronger than in mid-latitudes. The seminal works by Rodwell and Hoskins (1996; 2001; hearafter RH01) provide an elegant conceptual framework on how diabatic heating interacts with topography to establish a zonally asymmetric circulation in low-latitudes. In the idealized experiments of RH01, diabatic heating downstream of a mountain strengthens localized subsidence over upstream of the mountain via nonlinear interactions with the topography. As the insentropes intersect with the mountains, it is technically difficult to set up an analytical framework on how the mountains interact with the diabatic heating. Instead, RH01 suggests a conceptual framework using the Sverdrups' vorciticy balance: $\beta v \approx f \frac{\partial \omega}{\partial p}$. This equation simply indicates that the vertical stretching (shrinking) of vortex tube would be balanced by the poleward (equatorward) movement of the vortex tube (Gill 1982). In general, the vertical stretching by strong moist convection in downstream of a mountain is often

accompanied by the anomalous subsidence (or low-level anti-cyclonic motions) upstream of the mountain. The likely reason for this is that the convective heating generates westward propagating Rossby waves, which would stabilize the atmosphere in the upstream (Gill 1980; Chou and Neelin 2003).

Why Central Asian mountains? Comprehensive AGCM experiments consistently show that the Central Asian mountains (covering both the Tibetan Plateau and the Altai-Sayan mountains) explain a dominant portion of the topography-forced stationary waves during the Northern Hemisphere (NH) winter (Held et al. 2002). This is not surprising as the speeds of low-level jets impinging on the Central Asian mountains are quite high and the Indo-Western Pacific warm pool is located immediately downstream of the Tibetan Plateau. Furthermore, the Tibetan Plateau is known to tremendously affect the monsoon circulation and diabatic heating field during the NH summer (Hahn and Manabe 1975).

In this thesis, I hypothesize that a few major challenges in the Earth's atmospheric circulations could be explained by the stationary waves generated by the Central Asian mountains. In particular, I focus on understanding how the Central Asian mountains affect the (1) midwinter suppression of North Pacific storminess and the (2) onset of the South Asian summer monsoon. Recently, there have been important advances in these two topics, which directly motivate this thesis work. In particular, (1) a recent work by Son et al. (2008) found convincing evidence that mountains in mid-latitudes can weaken the downstream storminess by reducing the zonal traveling distance of wave packets. (2) A recent work by Boos and Kuang (2009) suggests that the surface heating over the Tibetan Plateau cannot be a major energy source for enhancing the monsoon circulation strength. Motivations for these two individual research topics will be further introduced in the subsequent sections in detail.

Latent heating is an essential ingredient for realistic simulations of the topography-forced stationary waves. Thus, it would be advantageous to use a comprehensive AGCM to understand the stationary waves as opposed to a dry model, although interpretations the results of GCMs are not clear-cut. To test the role of mountains in climate, the topography boundary conditions are removed or modified in various ways. Modifying the topographic boundary conditions in a comprehensive GCM affects almost every major element of the atmospheric circulations, such as wind speed, horizontal waveguide, vertically propagating waves and diabatic heating field. Keeping this in mind, the AGCM outputs will be carefully analyzed with clear physical basis in this thesis.

1.1. Midwinter Suppression of North Pacific Storminess

Extratropical storminess in the North Pacific exhibits peculiar characteristics; it is generally weaker in winter than in fall and spring although low-level baroclinicity is maximized in winter. This is so-called the midwinter suppression of the North Pacific storminess, which was first noted by Nakamura (1992). The mismatch between baroclinicity and storminess is against the classic theory by the linear Eady model of baroclinic storm formation and growth (Eady 1949; Lindzen and Farrell 1980). Discrepancies between theory and observations are quite common. What matters more would be whether we are asking a physically meaningful question. In general,

the midwinter suppression problem is regarded as a very challenging problem possessing rich physics. These include (i) do linear baroclinic eddy growth rate (i.e. baroclinicity) properly represent the actual baroclinic eddy growth rate (i.e. baroclinic conversion)? (ii) Does a weaker downstream eddy development lead to weaker downstream storminess? If so, what causes the weaker downstream eddy development over the North Pacific?

A substantial body of research exists that tries to address question (i). A notable theory for (i) is arguably the 'barotropic governor', which was first suggested by James (1987). Based on an idealized dry GCM experiments, James (1987) showed that baroclinic instability can be limited by barotropical wind shear. A series of idealized experiments by James (1987) indicate that a meridionally-confined westerly jet with intense jet core near the subtropics has relatively smaller baroclinic conversion (BCC) although baroclinicity is quite large. The 'barotropic governor' has been applied to the midwinter suppression problem with different methodologies (Nakamura, 1992; Harnik and Chang, 2004; Deng and Mak, 2005). Indeed, composite analysis of reanalysis data indicate that the suppression of the North Pacific storm activity is accompanied by the development of meridionally confined subtropical jet (Nakamura and Sampe 2002) or stronger mid-latitude jet (Chang 2001) over the Eastern Eurasian continent and the Western Pacific. However, they neglect that there is a monster in the Eurasian continent – the Central Asian mountains, which would make the mechanisms a lot more complicated. Different types of jets over the Eastern Eurasian continent may interact with the Central Asian mountains to produce different types of stationary waves and horizontal waveguide.

A recent work by Son et al. (2008) provides insight into how different background jets interact with a mountain in the mid-latitudes to alter the horizontal waveguide and the downstream eddy development. This work provides an important clue that the question (ii) – downstream eddy development – might be more directly related with the North Pacific storminess than the question (i) – barotropic governor. Downstream eddy development has been regarded as an influential factor for determining the global Eddy Kinetic Energy (EKE) distribution. Because of the downstream eddy development, the maximum upper-troposphere EKE and storminess tend to occur far downwind of the maximum baroclinicity (Vallis and Gerber 2008).

How well do we understand the downstream eddy development? The baroclinic eddy life cycle in a zonally-varying storm track is somewhat different from the classical life cycle (Lorenz 1955). In a storm track, the baroclinic eddy energy is always advected downstream – a decaying eddy gives up its energy to neighboring eddies downstream (Chang 1993; Orlansky and Chang 2000). The definition of the downstream eddy development traces back to the seminal work by Simmons and Hoskins (1979). Simmons and Hoskins (1979) specified a localized perturbation in a baroclinically unstable atmospheric model to examine how the disturbance develops downstream. They attempted to explain the downstream eddy development by the exponentially growing normal-mode. However, the real atmosphere is never in the zonally uniform state. Rather, at any given time, finite-amplitide eddies driven by a certain initial condition exist everywhere to provide a finite amplitude perturbation. In many cases, the non-normal eddy growth rate is much more rapid than the exponentially growing normal mode over some finite time period (Farrell 1984). Thus, it is hard to see an exponentially growing normal mode in the real atmosphere. Based on the idea of Farrell (1984), Zhang and Held (1999) specificed the transient eddies stochastically in their linear model with realistic surface boundary conditions. Surprisingly, the eddy momentum flux and many other essential dynamics are well simulated.

While we seem to understand the essential physics of the downstream eddy development, quantifying the strength of the downstream development in the real atmosphere has never been an easy thing to do. It is emperically known that the wave packets can be more zonally coherent when the background eddies are biased toward higher wavenumbers (Lee and Held 1991). However, it is unclear whether the zonal coherency of the wave packet is a good measure for the downstream eddy development. So far, statistical method such as regression or correlation has been used to measure the zonal coherency of the wave packet to infer the efficiency of downstream eddy development (e.g. Chang and Yu 1999). In Chapter 2, the efficiency of downstream eddy development is inferred from the zonal coherency of the wave packet calculated from the lagged correlation of 300 hPa eddy streamfunction. It is unclear if this correlation method can diagnose the downstream eddy development reasonably well.

1.2. Tibetan Plateau and the onset of the South Asian summer monsoon

The South Asian summer monsoon is consistently stronger in the presence of the Tibetan Plateau in many AGCMs (Hahn and Manabe 1975; Kutzbach et al. 1989; Yasunari et al. 2006; Boos and Kuang 2009). Previous studies suggest that the surface sensible or latent heat flux over the Tibetan Plateau is the fundamental source for strengthening the monsoon circulation (Yanai and Wu 2006; Luo and Yanai 1984). While the larger surface fluxes in the subtropics are certainly helpful for strengthening the monsoon, there is no clear evidence that the surface energy fluxes over the Tibetan Plateau are particularly larger than the ones in other subtropical monsoon regions. These previous studies also argue that heating in higher altitudes is particularly efficient in driving the monsoon circulation. A few studies interpret the upper-troposphere heating, such as the convective latent heating, as a heat source for driving the monsoon circulation (e.g. Webster et al 1998). It can be misleading to assume the upper-troposhere convective heating as an external heat source (Emanuel 1994).

Given that the Tibetan Plateau is not a magical material enhancing the surface energy fluxes, what else would be a factor? An anwer could come from considering interactions between tropics and the extratropics. The seminal work by Rodwell and Hoskins (2001) showed that tropical circulations are under strong influence of Rossby waves associated with the westerly winds in the extratropics. Indeed, idealized experiments using a Quasi-equilibrium Tropical Circulation Model (QTCM) found that the westward-propagating Rossby waves associated with the beta-plane effect may be an important factor limiting the northward progression of monsoon circulation (Chou and Neelin 2003). Furthermore, Chou and Neelin (2003) found that the ventilation (i.e., horizontal MSE advection) in the extratropics also limits the northward progression of monsoon, highlighting the extratropics as an important mediator for limiting the tropical monsoon circulation. An idealized, aquaplanet modeling study by Bordoni and Schenider (2008) provide an elegant and comprehensive theory on how extratropical eddies mediate the regime transition of the tropical monsoon circulation.

Even though rapid progress has been made in elucidating the mechanisms on how extratropics affect the tropical monsoon circulation, it was until recently still unclear why the Tibetan Plateau strengthens the monsoon. A recent modeling study by Boos and Kuang (2009) provides an answer – as a thermal insulator. As the Tibetan Plateau reduces cold-dry air advections from the extratropics, the subcloud layer entropy over India and the Arabian Sea can be maintained higher

than other areas of comparable latitudes. This idea is consistent with the idealized modeling study by Chou and Neelin (2003), which emphasizes the role of ventilation in the extratropics. Indeed, the narrow mountains surrounding the Northern India in the numerical simulations of Boos and Kuang (2009) turn out to effectively strengthen the monsoon rainfall and the low-level winds during the peak monsoon season (July-August).

What happens when the subtropical jet impinges on the Tibetan Plateau? The 'narrow mountains' in Boos and Kuang (2009) may well represent a thermal insulator during the peak monsoon season. However, it is still possible that the narrow mountains have their dynamical effect on monsoon during pre-monsoon season (April and May) or monsoon's onset (late May and early June) when the low-level westerly winds still exist over the South-Western Tibetan Plateau. In many cases, mountains in mid-latitudes refract waves south-eastward and generate low-level cyclonic motions downstream of the mountains – a linear response of stationary waves to orographic forcing (Held et al. 2002; Cook and Held 1992). The topographically-forced low-level cyclonic motion is known to decrease the near-surface pressure downstream of the topography in an aquaplanet configuration (Cook and Held 1992). I hypothesize that the remarkably strong moist convection over the Bay of Bengal during the pre-monsoon season or monsoon's onset could be driven by the topography-forced low-level cyclonic motions.

Chapter 2: The role of the Central Asian mountains on the midwinter suppression of North Pacific storminess

Abstract

The role of the Central Asian mountains on North Pacific storminess is examined using an atmospheric general circulation model by varying the height and area of the mountains. A series of model integrations shows that the presence of the Central Asian mountains suppresses North Pacific storminess by 20-30% during boreal winter. Their impact on storminess is found to be small during other seasons. While some of the changes in storminess arise from a reduction to the gravity-wave drag as mountain height is decreased, the larger effect comes from the pure topographic effect of mountain height.

Two main causes of the reduced storminess are diagnosed. First, the decrease in storminess appears to be associated with a weakening of downstream eddy development. The mountains disorganize the zonal coherency of wave packets and refract them more equatorward. As the zonal traveling distance of wave packets gets substantially shorter, downstream eddy development gets weaker, leading to the weakening of transient eddy kinetic energy and storminess. Second, the Central Asian mountains suppress the global baroclinic energy conversion. The decreased baroclinic energy conversion, particularly over the Eastern Eurasian continent decreases the number of eddy disturbances entering into the Western North Pacific. The 'barotropic governor' does not appear to be a dominant factor in explaining the results.

2.1. Introduction

Extratropical storminess in the North Pacific exhibits peculiar characteristics; it is generally weaker in winter than in fall and spring (e.g., RHS panel of Figure 2-1a) although low-level baroclinicity is maximum in winter (e.g., Figure 2-3a). This so-called midwinter suppression of the North Pacific storminess or storm track (hereafter midwinter suppression) was first noted by Nakamura (1992). A number of studies have proposed hypotheses based on both observational data and climate models. These include weakened eddy seeding-feeding processes associated with downstream development (Chang 2001; Zurita-Gotor and Chang 2005), advection by strong westerly jet (Nakamura 1992; Harnik and Chang 2004), barotropic wind shear effect (Deng and Mak 2005), trapping of the baroclinic waves in higher altitudes by stronger subtropical jet (Nakamura and Sampe 2002) and diabatic heating (Chang 2001). The definitive mechanism(s), however, still remain to be determined.

The role of downstream development of baroclinic wave packets has been intensively investigated (Simmons and Hoskins 1979; Lee and Held 1993; Orlansky and Katzfey 1991; Orlansky and Chang 1993; Chang and Orlansky 1993; Chang 1993; Hakim 2003) and applied to the midwinter suppression (Chang 2001; Zurita-Gotor and Chang 2005). By investigating the Eddy Kinetic Energy (EKE) budget of the eddy life cycle, Orlanski and Chang (1993) found that wave packets primarily decay by transferring energy downstream, specifically in the form of ageostrophic geopotential flux. Zurita-Gotor and Chang (2005) performed a number of experiments using a two layer quasi-geostrophic model by placing a strong eddy damping (or wave-packet barrier) in a limited region. It is found that localized eddy damping tends to reduce eddy amplitude over vast downstream areas and its recovery takes place over a long distance, specifically in the Northern Hemisphere (NH) winter condition when the basic flow has strong eddy group velocity.

Previous studies have suggested that the topography is important for the presence of the Pacific storm tracks (Lee and Mak 1993), but its quantitative impact has only been recently investigated (Son et al. 2009, hereafter S09). Using a dry atmospheric dynamical core model with imposed basic state, S09 found that a strong single jet (qualitatively similar to the jet over the Eurasian continent) has well-organized wave packets traversing the globe in few weeks. Eddies grew not only through local baroclinicity, but also by eddy seeding-feeding processes. This organized wave packet, having uniquely long zonal extent and temporal persistence, gets substantially shorter when idealized topography was introduced in mid-latitudes. It resulted in a localized storm track downstream of the topography whose intensity was much weaker than the one in the absence of the topography. They further showed that the topographic effect on storm track intensity is highly sensitive to background flow. When the background flow has weak double-jet pattern (qualitatively similar to the Atlantic jet), storm track intensity was instead slightly increased as it enhances local baroclinicity downstream of the topography. These results

suggested that the topographical impact on the two different storm tracks in the Northern Hemisphere, the Pacific and Atlantic storm track, might be very different.

This study is also motivated by the observational studies of Penny et al. (2009). Using reanalysis data, Penny et al. (2009) found that Central Asia (including the Siberia) is the area where the suppression of eddy seeding occurs. Their Lagrangian tracking methods revealed that the amplitude and frequency of cyclogenesis in the lee of the Central Asian mountains reduces in winter, whereas the local amplitude and frequency of cyclogenesis over the Western Pacific did not decrease, suggesting that the reduced eddy seeding from the Central Asia and the Siberia is a key factor in midwinter suppression of the North Pacific storminess.

In light of the above studies, we investigate the role of the Central Asian mountains on North Pacific storminess using a comprehensive atmospheric general circulation model (AGCM). It has merit over the simple models used by Zurita-Gotor and Chang (2005) and S09 in that the AGCM incorporates realistic atmospheric physics and boundary conditions, and simulates a realistic atmospheric circulation. For instance, the wave packets simulated by S09 are much more coherent and persist much longer than the observations (Son et al. 2008); this does not occur in the AGCM. In addition, an AGCM with realistic topography and land-sea geography may allow us to identify relevant mechanisms that cannot be captured in idealized models.

2.2. Model and Analysis Method

We used the Community Climate Model 3.10 (CCM3; Kiehl et al, 1998) at T42 horizontal resolution and standard 18 levels in the vertical. In this study, monthly-varying climatological surface boundary conditions such as land surface type, sea surface temperatures (SSTs) and sea ice, are prescribed in the model. The climatological montly mean SSTs are calculated from the 40 years' monthly mean Reynolds optimum interpolation data (Reynolds et al. 2002), spanning from 1960 to 2000.

In all model integrations, the same boundary conditions are used except for topography over Central Asia, which are gradually reduced from high-latitudes to mid-latitudes as summarized in Table 2-1. The control experiment, hereafter labeled M100, maintains all the mountains at present-day heights (Figure 2-1a). In the M75 experiment, we reduced the height of the Altai-Sayan mountains (covering 55E-115E and 42N-55N) by 95% from their original heights (Figure 2-1b), while mountain heights from 42N to 37N are reduced gradually so that they merge smoothly with the unaltered topography south of 37N. In the M50 experiment, we further removed the northern part of the Tibetan Plateau. Latitudes north than 37N is reduced by 95%, while the transitional regions from 32N to 37N are similarly reduced to merge smoothly with the unaltered topography south of 32N (Figure 2-1c). The entire Tibetan Plateau area is further reduced in the M20 experiment, retaining only the southern part of the Tibetan Plateau, Himalaya (Figure 2-1d). It should be noted that the imposed sub-grid variability of the mountain

height, which is used for the gravity wave drag parameterization, has also been reduced with mountain height (so by 95% if the mountain height is reduced by 95%).

To separate the role of the gravity wave drag associated with the sub-grid variability of the Central Asian mountains, from the effect of mountain height, we conducted an additional series of experiments. While we fix the height of the Central Asian mountains to present-day, we gradually reduced the sub-grid variability of the mountains from high-latitudes to mid-latitudes. The areas of reduction are consistent with the previous experiments, which are summarized in Table 2-1.

Table 2-1 AGCM design of experiments (main experiments)

Experiments	Descriptions	Topography boundarie
M100	Control experiment with full topography	Figure **2-1a**
M75	Altai-Sayan mountains (42-55N; 55-120E) are reduced by 95%. The latitudes of 37-42N are gradually recovered.	Figure **2-1b**
M50	Altai-Sayan mountains including the northern part of the Tibetan Plateau (37-55N; 55-120E) are reduced by 95%. The latitudes of 32-37N are gradually recovered.	Figure **2-1c**
M20	Altai-Sayan mountains and the most part of the Tibetan Plateau except the Himalaya are reduced by 95%	Figure **2-1d**

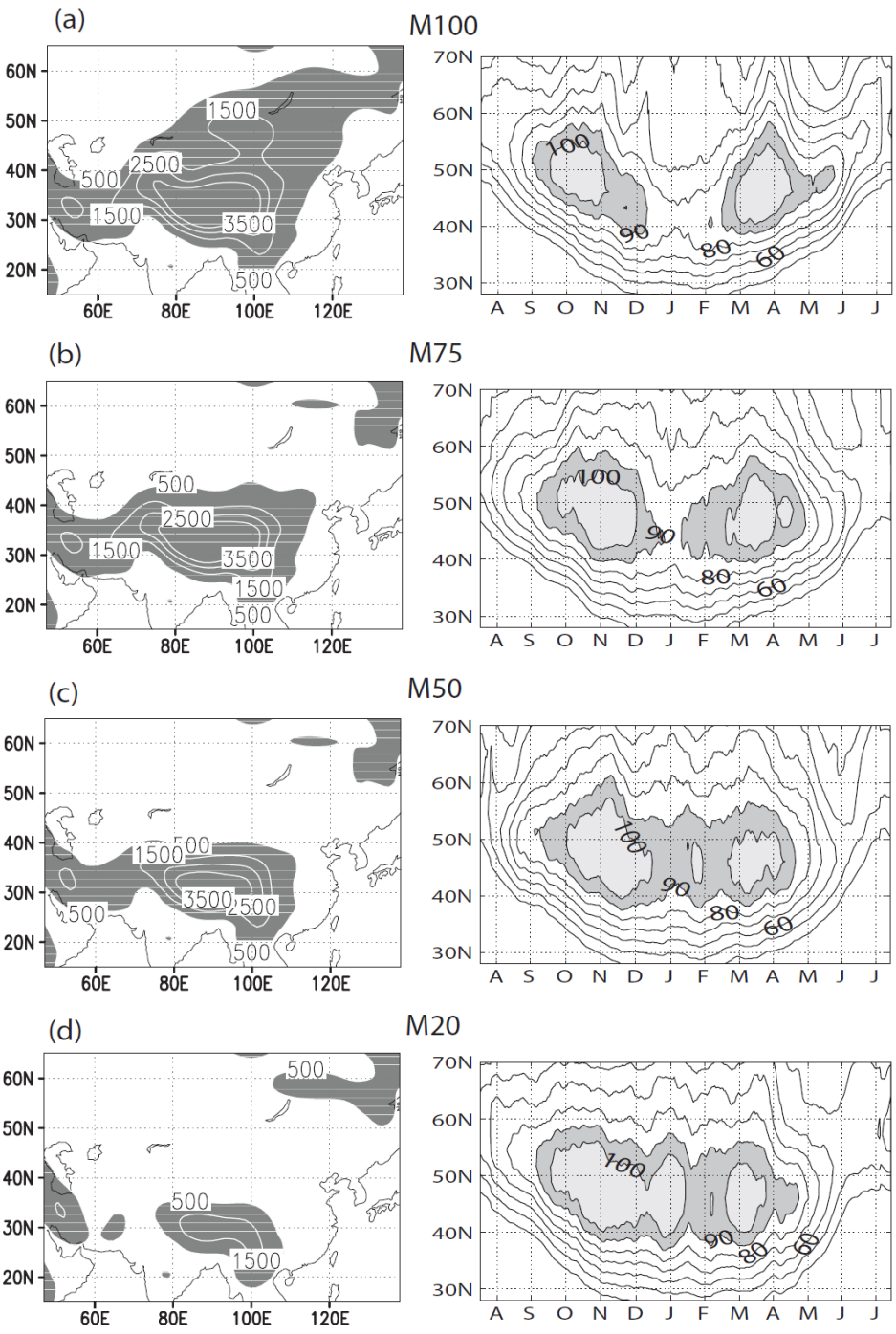

FIG. 2-1: The left hand panels are the boundary conditions for the CCM3 simulations. Mountains higher than 500 m are shaded. The right hand panels show the seasonal march of the upper-level (300hPa) North Pacific storminess (unit in meters) averaged between 140E and 140W, for the (a) M100, (b) M75, (c) M50 and for the (d) M20 experiments.

Each experiment ran for 22 years, and last 18 years are used for the analysis. As climatological monthly-mean SSTs are prescribed, 4 years of integration was sufficient for spin-up. We used daily mean output to calculate time-mean flow and various eddy statistics, such as storminess, eddy heat flux and baroclinic energy conversion (BCC). The low-level baroclinicity is measured by Eady parameter, $\frac{f}{N}\left(\frac{dU}{dz}\right)$, where f and N represent the coriolis parameter and vertical static stability, respectively. It is evaluated at 780 hPa, and using a finite difference method between two adjacent vertical levels (i.e. 700 hPa and 850 hPa) to evaluate the vertical wind shear. The storminess, or storm track intensity, is defined as 8-day high-pass filtered upper-level (300hPa) geopotential height variations, similar to the method used by Nakamura (1992). The resulting high-frequency signal has been smoothed by a 20-day running mean, and the smoothed data averaged to produce the annual mean. The BCC is calculated using the equation in Peixoto and Oort (1992), $\int_{MT}^{TOA} \omega'\alpha' dp$, where ω' and α' denote transient pressure velocity and specific volume, respectively; MT and TOA indicate the Mountain Top (or surface) and the Top of Atmosphere. Both ω' and α' are filtered by using 8-day high-pass filter[1] to exclude low-frequency eddies. Since the resulting BCC might be dependent on the filtering method, we also calculated the unfiltered BCC, $\int_{MT}^{TOA} (\omega - [\omega]) \cdot (\alpha - [\alpha]) dp$, where bracket denotes zonal-mean climatology. We found that the BCC calculated from the 8-day high-pass filtered eddies explain about 65% of the total unfiltered BCC. In the case when the 20-day high-pass filtered eddies are used, the filtered transient BCC explains more than 80% of the total unfiltered BCC.

The Eddy Kinetic Energy (EKE), $u'^2 + v'^2$, is computed using daily zonal and meridional wind fields. The seasonal cycle, derived from 18-year daily climatology and smoothed with 20-day running average, is first removed from the data. The EKE spectrum is then partitioned into transient and stationary (including quasi-stationary) EKEs. The former is calculated by using 8-day high-pass filtered eddy fields[1] whereas the latter is defined with low-pass filtered (longer than 100 days) eddies. Strictly speaking, the stationary EKE we defined includes the quasi-stationary or some low-frequency transient EKE.

[1] As the storminess has been defined by 8-day high-pass filtered geopotential height, we consistently used 8-day high-pass filter for the calculations of transient BCC and transient EKE. However, 20-day high-pass filter is more widely-used for calculating the transient eddies. We also calculated transient BCC and transient EKE using 20-day high-pass filters to check the robustness of our interpretations. We found that both 8- and 20-day high-pass filtered transient eddies provide qualitatively consistent results.

2.3. Sensitivity of the North Pacific storminess to the Central Asian mountains

The response of the low-level eddies to the mountains would be different from the upper-level eddies because the upper-troposphere has faster eddy group speed, conveying the upstream disturbances more efficiently. Reanalysis data shows that the midwinter suppression of North Pacific storminess is much weaker in the lower-troposphere than in the upper-troposphere (Nakamura 1992). In light of this, we first examine how the upper and the low-level eddies respond to the mountains. Seasonal progression of the upper-level storminess is shown in section (a) and that of low-level eddy activities are examined in section (b). We will particularly focus on the differences between the M100 and M50 experiments, since the midwinter suppression is largely gone (although slight suppression still exists) by the M50 experiment.

2.3.1. Seasonal march of the upper-level storminess

The M100 (control) experiment captures midwinter suppression of the North Pacific storminess (Figure 2-1a) and the wintertime baroclinicity maximum (Figure 2-3a) reasonably well. The storminess has a maximum in October and rapidly decays from November until it is greatly suppressed in midwinter. On the other hand, baroclinicity has a single maximum strength in winter, consistent with previous results.

The wintertime storminess gradually increases as the area and height of the Central Asian mountains decrease (Figures 2-1a). The distinct double maximum signal almost disappears when the entire Altai-Sayan Mountains are removed and the Tibetan Plateau is substantially reduced (M20 in Figure 2-1d). Interestingly, the North Pacific storminess during fall or spring rarely responds to the mountains. Using a series of idealized model integrations, S09 showed that storminess is sharply decreased by a mountain when background westerly is a strong single-jet state. However, only minimal sensitivity is found if background westerly is a weak double-jet state. Figure 2-2 shows the longitudinally averaged zonal wind over the Central Asia (from 60E to 100E) in January and October. While the January jet profile is reminiscent of a single jet, the October jet is qualitatively similar to weak double-jet state in S09. Thus, the results of S09 appear applicable to interpreting our situation.

To further investigate storm-track sensitivity to the background flow, we examined storminess over the North Atlantic after reducing the area and height of the Rocky Mountains. Unlike the Eurasian continent, the wintertime westerly jet over the Eastern Pacific and North America is broad, although not as broad as the double-jet state in S09. The wintertime storminess over the North Atlantic increases only by 5% when the Rockies are removed (not shown). This is again consistent with the findings of S09.

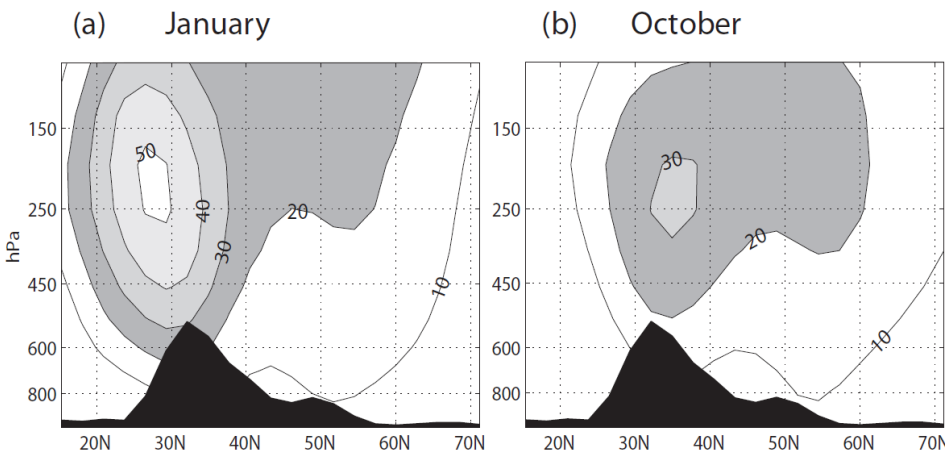

FIG. 2-2. Zonal wind averaged over the longitudinal interval of 60E to 100E for (a) January, (b) October simulated by CCM3.

2.3.2. Seasonal march of low-level baroclinic eddy activities

As addressed above, the seasonal evolution of the baroclinicity has a single wintertime maximum (LHS of Figure 2-3a) and the structure remains almost unchanged even after the entire Altai-Sayan mountains are removed (RHS of Figure 2-3a). Rather, the wintertime baroclinicity "weakens" over 30N-45N in the absence of the Altai-Sayan mountains even though the storms get stronger (Figure 2-1c). Note that baroclinicity is based on the linear theory and does not necessarily indicate the behavior of actual baroclinic eddy activities, which can be highly nonlinear.

To better understand the puzzling relationship between upper-level storminess and lower-level baroclinicity, we define the baroclinic eddy activities by the baroclinic energy conversion (BCC). In the M100 control experiment, the BCC exhibits a slight suppression in midwinter relative to its shoulder seasons (LHS of Figure 2-3b). Similarly, 700 hPa eddy heat flux exhibits a similar mild midwinter suppression (now shown). However, the magnitude of suppression is much weaker than that of the upper level, which is consistent with reanalysis data (Nakamura 1992). When the Altai-Sayan mountains and the Northern Tibetan Plateau are removed, the BCC is somewhat enhanced in boreal fall and winter, especially during November and December (RHS of Figure 2-3b). While a hint of midwinter minimum still exists, midwinter BCC increases up to 20%. Note that the M50 experiment exhibits enhanced eddy activities over the high-latitude regions (50-60N), indicating that the mountains tend to meridionally confine baroclinic eddy activities southward.

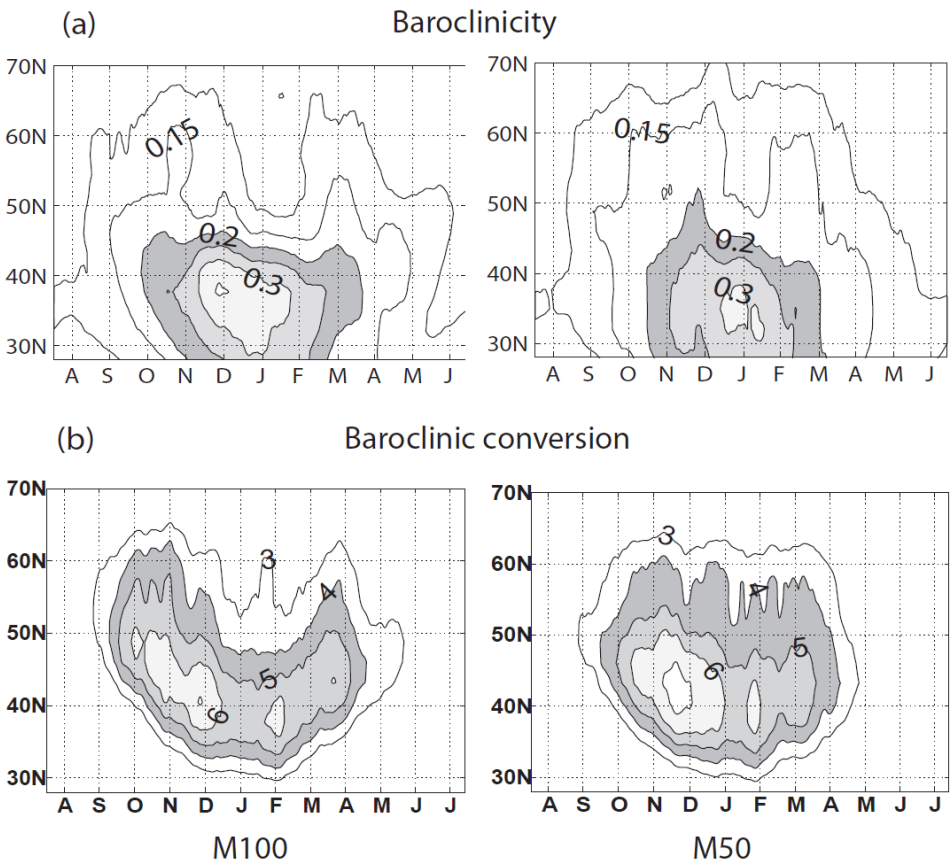

FIG. 2-3: (a) Seasonal march of the low-level baroclinicity (day^{-1}) and (b) baroclinic conversion ($W\ m^{-2}$) over the North Pacific, averaged between 140E and 140W. The left-hand side panels are for M100 and the right-hand side pales are for M50.

2.4. Baroclinic energy conversion and the upper-troposphere storminess

In this section, we further elucidate the possible linkage between the lower and the upper-level eddy activities. We first examine the global anomalous patterns of storminess and BCC caused by the mountains in section (a). Their possible relationships are further investigated and discussed in section (b).

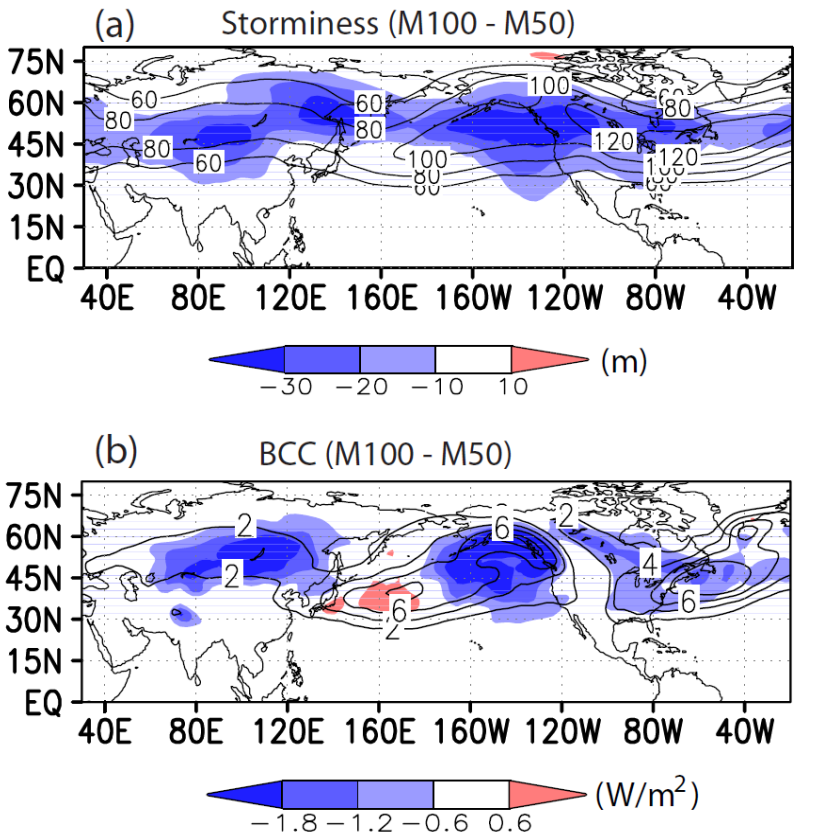

FIG. 2-4: Midwinter (Dec-16 to Feb-15 mean), anomalous (a) 300 hPa storminess (shadings: meters) and (b) baroclinic conversion (shadings: W m^{-2}) calculated from the differences between M100 and M50 (M100-M50). The contour lines indicate climatological mean (a) storminess and (b) baroclinic conversion for M50.

2.4.1. Altered midwinter storminess and BCC

Figure 2-4a shows the response of the NH midwinter storminess to the Altai-Sayan mountains and the Northern Tibetan Plateau (M100-M50). The "midwinter" refers to 60 days annual-mean from Dec-16 to Feb-15. It can be seen that the mountains affect storminess not only near-downstream of the mountains but also far-downstream, indicating that the mountains modify eddy activities through the whole hemisphere. Over the Eastern Eurasian continent, storminess decreases more than 30 m (shadings of Figure 2-4a) which is about 40% of the background storminess of M50 (contours of Figure 2-4a). The North Pacific also experiences pronounced weakening of storminess, up to about 30%.

The changes in the upper-level eddy activities are further examined by partitioning the reduced storminess into the changes in amplitude and the frequency of storminess. Note that reduced storminess could result from weaker amplitude of individual storms and/or less frequent development of storms. The standard deviation of the geopotential height at 300 hPa in the NH

mid-latitudes during midwinter is about 120m in the control experiment (M100). We arbitrary set the deviation of 140m, slightly larger than climatological standard deviation, as the threshold value of a storm event[2]. The storm events passing this threshold are used to measure storm amplitude and frequency. The amplitude is quantified by averaging anomalous geopotential height for those events. The frequency is estimated by counting the number of events. To avoid over-counting associated with consecutive perturbations, consecutive perturbations occurring within 5 days are counted as a single event.

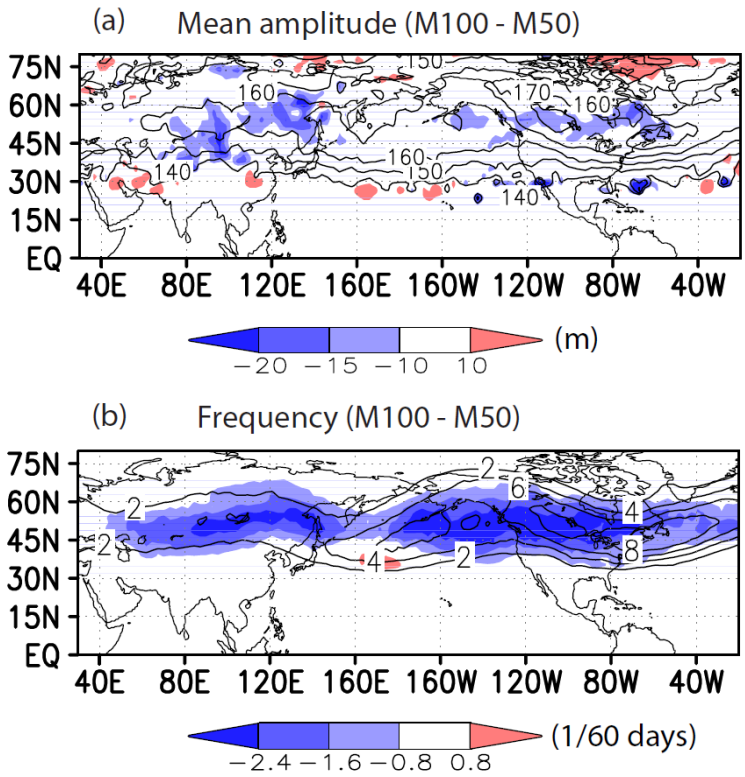

FIG. 2-5: Midwinter (Dec-16 to Feb-15 mean), anomalous (a) mean-amplitude (shadings: meters) and (b) frequency (shadings: 1/60 days) of 300 hPa storminess calculated from the differences between M100 and M50 (M100-M50). See the text for the details on defining the amplitude and frequency. The contour lines indicate climatological mean (a) mean-amplitude and (b) frequency for M50.

Figure 2-5 shows differences of storm amplitude and frequency between the M100 and M50 experiments. A simple visual comparison of the anomalous amplitude and frequency indicates

[2] The fractional changes in the amplitude and frequency of storm activities are somewhat sensitive to the threshold value. However, for any given threshold we find that frequency has consistently much larger impact than amplitude.

that decrease in frequency is a main factor for weakening the storms in the presence of full topography. The storm frequency reduces up to 40% over the vast mid-latitude areas (Figure 2-5b) and the spatial pattern is consistent with the anomalous storminess (Figure 2-4a). On the other hand, the amplitude change is less than 10% from the mean (Figure 2-5a).

While the decrease in storminess or storm frequency persistently occurs over the whole NH extratropics, the reduction of BCC occurs somewhat sporadically (Figure 2-4b). It does not necessarily mean that the upper-level storminess is not influenced by lower-level eddy activities. Reanalysis data consistently exhibit that the maximum EKE in the upper troposphere is located downstream of the maximum baroclinicity in the mid-troposphere (Vallis and Gerber 2008). Considering that BCC is tied up with baroclinicity (i.e., linear eddy growth rate), the maximum storminess may occurs somewhere downstream of the maximum BCC. Therefore, the decreased BCC over the Eastern Eurasian continent (Figure 2-4b) might contribute to decreasing the North Pacific storminess (Figure 2-4a).

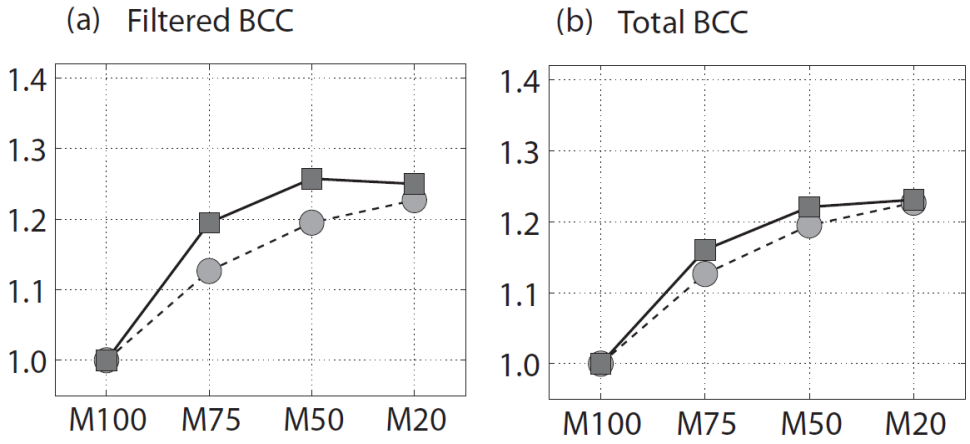

FIG. 2-6: Sensitivities of mid-latitude (32N-67N), zonal-mean fractional changes of (a) high-pass filtered BCC (square with solid line) and the (b) unfiltered total BCC (square with solid line) to the varying Central Asian mountains. The zonal-mean fractional changes of 300 hPa storminess are plotted as circle with dotted lines for comparison.

Figure 2-6 shows how global BCC and storminess respond to decreasing Central Asian mountains. Fractional changes of BCC generally keep pace with those of storminess, suggesting strong connection between these two variables. It should be noted that the relationship between BCC and storminess presented in Figure 2-6 is not completely linear. The high-frequency BCC of M50 is slightly stronger than that of M20 (Figure 2-6a). Storminess in the former, however, is weaker than in the latter. A qualitatively similar result, e.g., saturation of BCC, is found in the

unfiltered BCC (Figure 2-6b). This result suggests that there are some other mechanisms, which can explain the increase in wintertime storminess to decreasing Central Asian mountains.

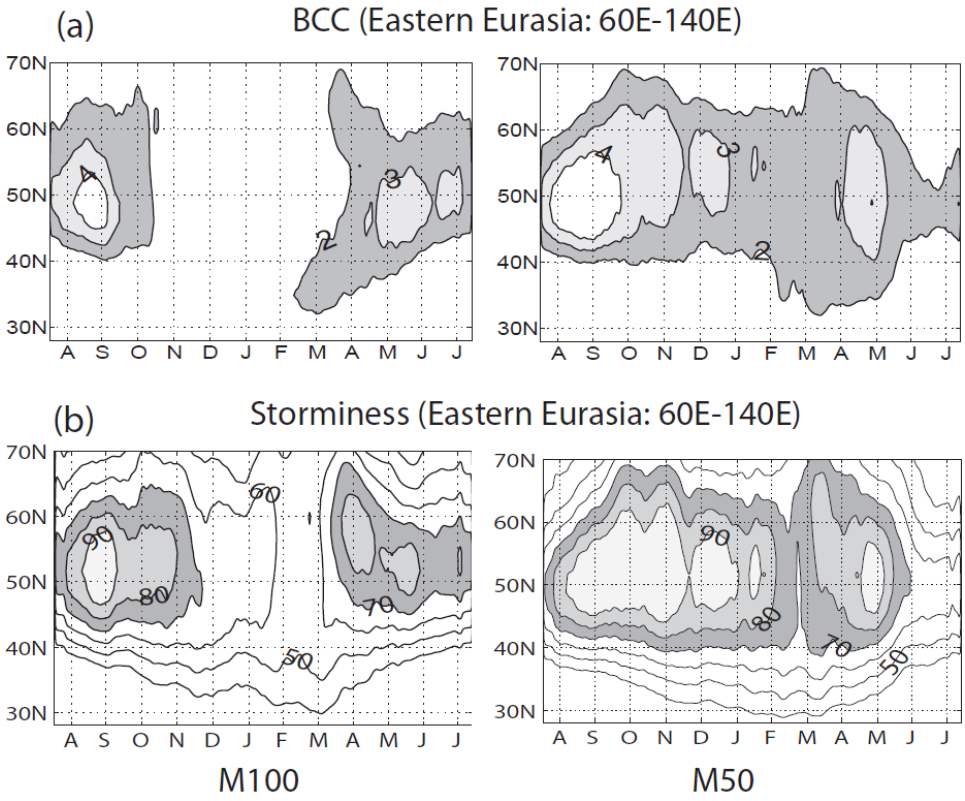

FIG. 2-7: The seasonal march of (a) baroclinic conversion (W m^{-2}) and (b) 300 hPa storminess (meters) over the Eastern Eurasian continent (60E-140E mean). The left-hand side panels are for M100 and the right-hand side panels are for M50.

2.4.2. Possible impact of the upstream BCC on downstream storminess

The seasonal evolution of BCC over the Eastern Eurasian continent exhibits much clearer wintertime suppression of wave activities than the North Pacific. The LHS of Figure 2-7a indicates that the Eastern Eurasian continent (60E-140E) experiences dramatic suppression of BCC in winter when the full mountains are imposed in the model (M100). The maximum BCC occurs in the late summer or early fall, up to 4.5 W/ m^2, and then rapidly decreases down to 2 W/ m^2 in November. In midwinter, it is only around 1 W/ m^2 or even less than one. Similarly, seasonal march of the upper-level storminess shows a distinct midwinter minimum (LHS of Figure 2-7b). In the absence of the Altai-Sayan mountains and the Northern Tibetan Plateau (M50), the BCC over the Eastern Eurasian continent is substantially enhanced in winter (RHS of

Figure 2-7a). Although a double maximum signal (maximum BCC in late fall and early spring) still exists, wintertime BCC of M50 is more than 100% stronger than that of M100. Likewise, the upper-level storminess of M50 exhibits much weaker midwinter suppression signal (RHS of Figure 2-7b) than that of M100.

Since the eddy group velocity substantially increases and the traveling distance of wave packets gets much longer in winter (Zurita-Gotor and Chang 2005), this increase (decrease) in BCC over the Eastern Eurasian continent might effectively strengthen (weaken) the North Pacific storminess. This argument is consistent with Penny et al (2009), also with Zhang and Held (1999). Zhang and Held (1999) demonstrate, using a linear model framework with stochastically-forced eddies, that the enhanced eddy (temperature or vorticity) forcing over the Central Asia can strengthen the North Pacific storminess.

What causes such a radical suppression of wintertime BCC over the Eastern Eurasia continent? Penny et al (2009) suggests that the strong near-surface static stability over Siberia could be a key factor for reducing the frequency and amplitude of cyclogenesis in boreal winter. Based on this idea, we calculated the near-surface static stability over the Eurasian continent both for the M100 and M50 experiments. While the near-surface static stability is substantially high in boreal winter over the Eastern Eurasian continent, there are minimal changes to it after the Altai-Sayan mountains and the Northern Tibetan Plateau are removed (not shown), suggesting that local BCC may not be always dependent on the near-surface static stability. In chapter 2.6, we will further discuss why the Altai-Sayan mountains can effectively decrease BCC, especially over the Eastern Eurasian continent.

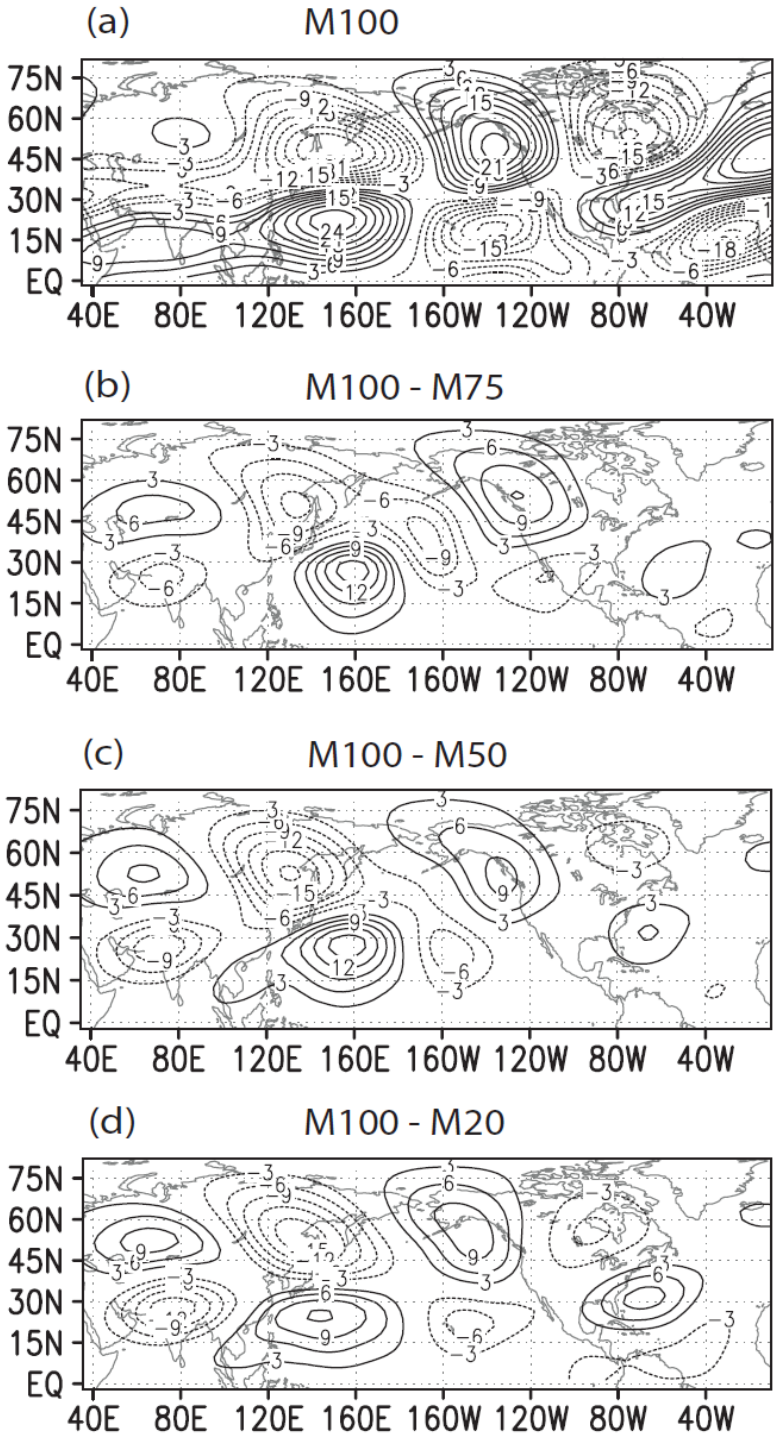

FIG. 2-8: The 300 hPa eddy streamfuction for (a) M100 in January. (b), (c), (d) are anomalous eddy streamfunction calculated from the differences between M100 and others; (b) M100-M75, (c) M100-M50, and (d) M100-M20 in January. The contour interval is $3x10^6$ m^2 s^{-1}

2.5. Stationary waves and baroclinic wave packets

The most pronounced impact of the Central Asian mountains on the NH winter circulations is the generation of stationary waves. The mountain-induced stationary waves would affect the transient eddies by redistributing the EKE spectrum (Yu and Hartmann, 1995). Since the upper-level storminess has been defined by high-pass filtered geopotential height, the decrease in transient EKE in the presence of the mountains may have a direct relationship with the decrease in storminess.

2.5.1. Stationary waves and the EKE spectrum

The linear wave response of the upper-tropospheric flow to the Tibetan Plateau is known to be limited in regional scale (Held et al., 2002), probably because of various damping effects, such as Ekman damping. The nonlinear response, however, is known to occur over the wide downstream areas as the Tibetan Plateau modifies the diabatic heating field (Held et al., 2002).

Figure 2-8a shows 300 hPa eddy streamfunction in January, simulated by the M100 experiment. Here, "eddy" denotes the deviation from the zonal mean. The simulated stationary waves have wavenumber-2 patterns, and their amplitudes are quite similar to observations (e.g. Figure 1a of Held et al. 2002). The anomalous eddy streamfunctions in the other experiments – deviations from M100 - are displayed in Figures 2-8b, 2-8c and 2-8d (M100-M75, M100-M50 and M100-M20). In all simulations, anomalies are found over the entire NH. It is worth noting that the magnitude of the anomalous stationary wave response is comparable in all three cases (Figures 2-8b, 2-8c and 2-8d), although the M100-M20 exhibits slightly wider stationary wave response than others (M100-M75 and M100-M50). The addition of the Altai-Sayan mountains to the Tibetan Plateau efficiently enhance the amplitude of stationary waves. It will be interesting to further examine why the mountains in higher latitudes (above 45N) are so efficient in exciting the wintertime stationary waves.

The magnitude of the stationary waves excited by the Altai-Sayan mountains are significant relative to the total stationary waves (compare Figures 2-8a and 2-8b). The EKE spectrum is hence likely to be modified by the mountains as well. Figure 2-9 shows the EKE difference between the M100 and M50 experiments during midwinter. As expected, transient EKEs are reduced over wide range of mid-latitudes (Figure 2-9a), whereas stationary and quasi-stationary EKEs are substantially enhanced (Figure 2-9b). The spatial pattern of reduced transient EKEs is quite similar to that of storminess (Figure 2-4a). The zonal-mean fractional changes of transient EKEs in all experiments keep pace with those of the upper-level storminess (Figure 2-12a). The linear relationship between the transient EKE and storminess still holds if a 20-day high-pass filter is used to calculate the transient EKE (not shown). This result suggests that the decreased

transient EKE change is strongly tied with the midwinter suppression. This result is somewhat different from S09 who found much weaker sensitivity of transient EKE to the mountain heights.

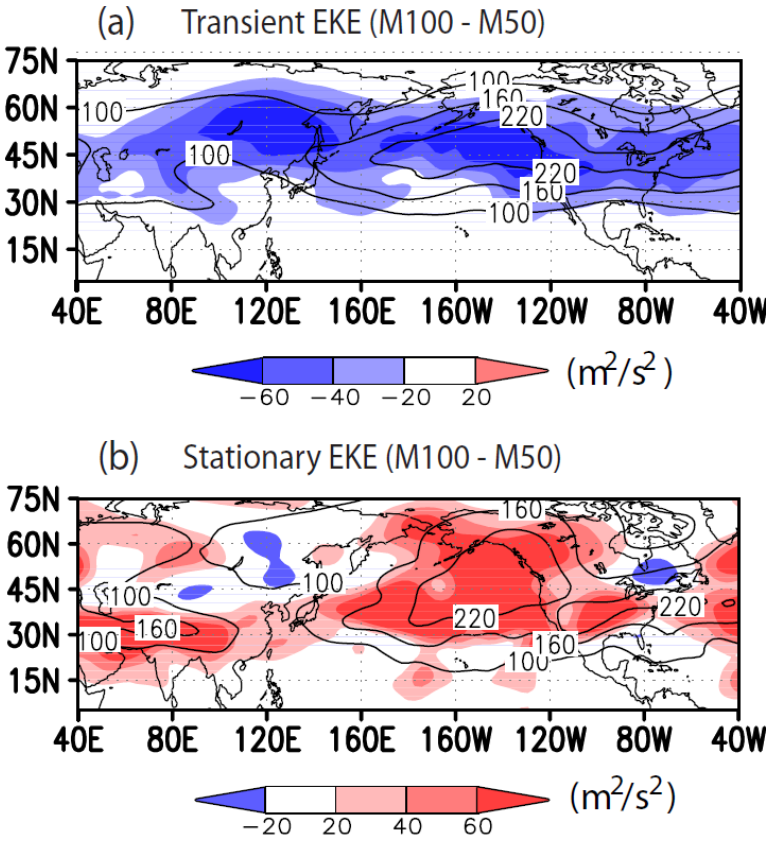

FIG. 2-9: Midwinter (Dec-16 to Feb-15 mean), anomalous (a) 8-day high-pass filtered transient EKE (shadings: $m^2\ s^{-2}$), and (b) 100-day low-pass filtered stationary EKE (shadings: $m^2\ s^{-2}$) calculated from the differences between M100 and M50 (M100-M50). The contour lines indicate the climatological mean, midwinter (a) transient EKE (b) stationary EKE for M50.

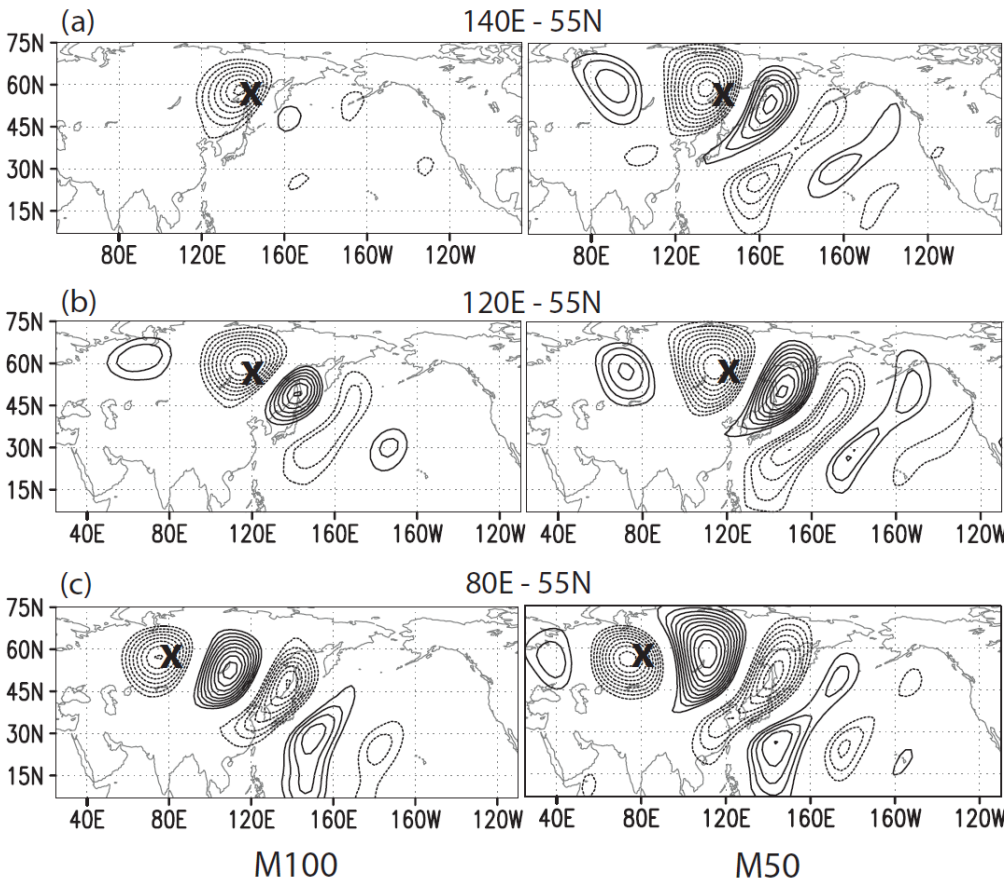

FIG. 2-10: One-point 2 days lag correlation of the 8-day high-pass filtered eddy streamfunction at 300 hPa for M100 (LHS panel) and for M50 (RHS panel). The contours are correlation coefficients at lag 2 days, which corresponds to 2 days after from the position of (a) 140E, 55N, (b) 120E, 55N and (c) 80E, 55N (these positions are indicated as X). The values higher than 0.2 or lower than -0.2 are contoured with each interval of 0.05.

2.5.2. Wave packet structure

What causes the zonally-extensive reduction of transient EKEs in Figure 2-9a? To answer this, we consider the zonal propagation of baroclinic wave packets and the associated downstream development of transient eddies. The structure of wave packets can be inferred by calculating the one-point lag or lead correlations of the eddy streamfunction (Chang and Yu 1999; S09). The eddy streamfunction is calculated by 8-day high-pass filtered streamfunction to capture the transient eddy of interest. A reference gridpoint is chosen, and correlation coefficients are computed against all other grid points in the NH with 2 days time lag.

Figures 2-10a and 2-10b show the structure of wave packets over the Western North Pacific (140E, 55N) and over East Asia (120E, 55N) individually. Wave packets in the M100 and M50 experiments are significantly different; while the wave packets in M100 are zonally restricted,

those in M50 have wider zonal extent. Furthermore, the wave packets of M100 refract more equatorward compared to M50. This result resembles Penny et al (2009) and Hakim (2003) who found that a large fraction of wave packets upwind of the Tibetan Plateau refract into the subtropics. Unlike the Western Pacific or East Asia, wave packets over Central Asia (80E, 55N: Figure 2-10c) are only weakly sensitive to the mountains. This is in contrast to Robinson et al (2006) who found distinct differences in the waveguide over Central Asia between years when the midwinter suppression is strong and weak. It is likely that interannual variability in the waveguide depends on the variability of the background zonal flow. In this paper, since we are focusing on the climatological mean response of waveguide to different topographic conditions, the interannual analog does not apply.

To better understand changes in the structure of wave packets, the zonal extent (coherence) of wave packets are quantified following S09. As in Figure 2-10, a 2-day lag correlation is computed for each reference gridpoint; the zonal extent between this reference point and the farthest gridpoint with correlation coefficient higher than a threshold value[3] (chosen to be 0.35) becomes the measure of the zonal extent for that reference point. The correlation field was slightly smoothed using Gaussian smoothing before measuring the zonal extent. This operation is done over all gridpoints, producing a hemispheric-wide map of zonal extent of wave packets. Figure 2-11 shows the differences of wave-packet extent between the M100 and M50 experiments. The decrease in wave-packet extent is evident over the vast mid-latitude storm track areas covering the North Pacific and the North America. More importantly, the overall pattern is qualitatively similar to that of storminess (Figure 2-4a) and storm frequency (Figure 2-5b). Figure 2-12b further shows that the zonal-mean fractional changes of wave-packet extent keep pace with those of storminess in all experiments. This result suggests that the reduced efficiency of downstream eddy development is an important ingredient for the midwinter suppression in our model.

[3] The zonal extent of wave packets is somewhat sensitive to the choice of threshold value particularly when the threshold value is small. For example, if the threshold value is less than 0.2, the subtropics exhibit longer zonal extent of wave packet than the mid-latitude. It is likely to be an artifact associated with the reflection of eddies from the tropics to the extratropics.

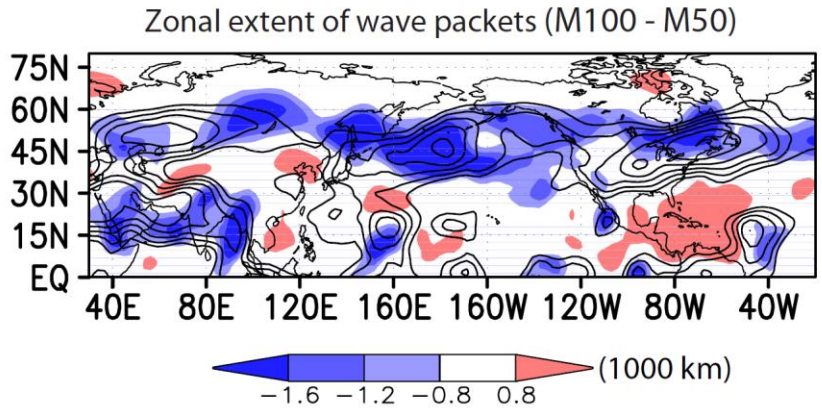

FIG. 2-11: Midwinter (Dec-16 to Feb-15 mean), anomalous longitudinal traveling distance of wave packets (shadings: 1000 km) calculated from differences between M100 and M50 (M100-M50). The contour lines indicate climatological mean longitudinal traveling distance of wave packets for M50. Contour starts from 3000 km with each interval of 500 km.

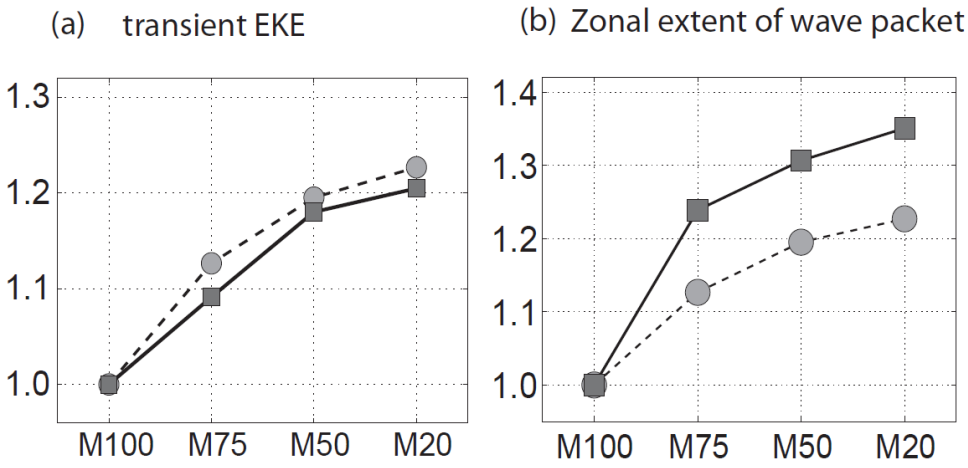

FIG. 2-12: Sensitivities of mid-latitude (32N-67N), zonal-mean fractional changes of (a) 8-day high-pass filtered transient EKE (square with solid line) and the (b) zonal extent of wave packets (square with solid line) to the varying Central Asian mountains. The zonal-mean fractional changes of 300 hPa storminess are plotted as circle with dotted lines for comparison.

2.6. Other possible mechanisms

It is still unclear why global BCC decreases as the Central Asian mountains increase. James (1987) showed that baroclinic instability can be limited by barotropical wind shear. The 'barotropic governor' has been applied to the midwinter suppression problem with different methodologies (Nakamura, 1992; Harnik and Chang, 2004; Deng and Mak, 2005). It is beyond

the scope of this study to fully investigate the barotropic governor process. Instead, we will briefly diagnose the possible relationship between BCC and barotropic wind shear in our AGCM experiments. We also discuss the sensitivity of our results to the magnitude of gravity wave drag associated with the sub-grid variability of mountains.

2.6.1. Barotropic governor effect

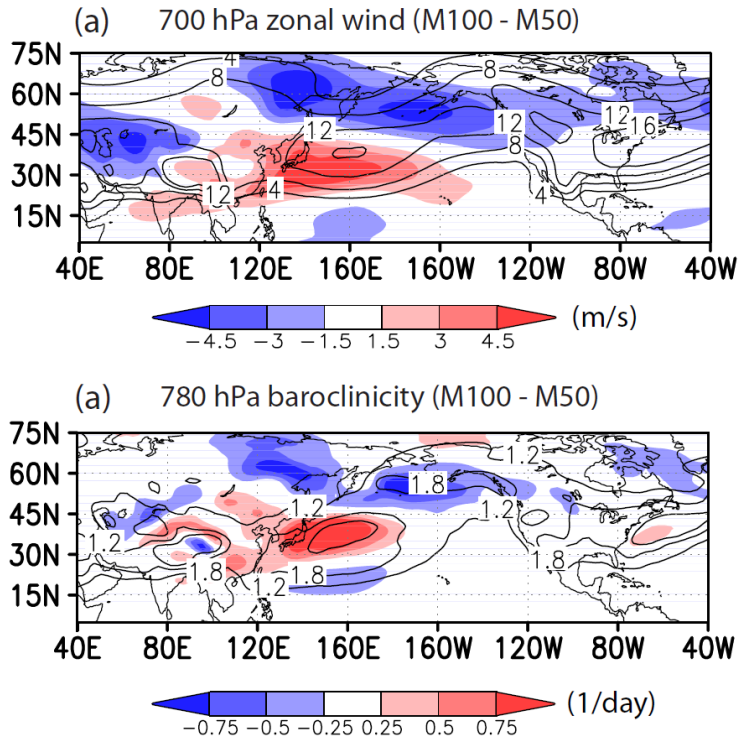

FIG. 2-13: Midwinter (Dec-16 to Feb-15 mean), anomalous (a) 700 hPa zonal wind speed (shadings: m s^{-1}) and (b) 780 hPa baroclinicity (shadings: day^{-1}) calculated from differences between M100 and M50 (M100-M50). The contour lines indicate the climatological mean (a) 700 hPa zonal wind speed and (b) 780 hPa baroclinicity for M50.

Figure 2-13a shows the altered zonal winds at 700 hPa (regarded as a steering level[4] for transient eddies) resulting from the removal of the Altai-Sayan mountains and the Northern

[4] The state of the low-level westerlies, steering the low-level ridges and troughs would be an important basic state modulating the downstream eddy propagation. 700 hPa level is often referred to as a steering-level, where westerly winds bear a direct relationship to the velocity of low-level disturbances. In a previous study, a simple mean of the 500 hPa and the 1000 hPa level (which roughly represent the 700 hPa level) westerly is used to identify the position of storm tracks over the North Pacific (Nakamura1992).

Tibetan Plateau (M100-M50). Strengthening of subtropical westerlies (25N-40N) and weakening of mid-latitude westerlies (45N-65N) are clearly seen in the Western North Pacific (shadings of Figure 2-13a), indicating that the westerlies are restricted to more equatorial latitudes when the mountains are present. The equatorward confinement of low-level westerlies is accompanied by the weakening (strengthening) of low-level meridional temperature gradient in mid-latitudes (subtropics). Figure 2-13b shows that the low-level baroclinicity, which is directly related with the meridional temperature gradient, gets weaker (stronger) over the mid-latitude (subtropical) North Pacific[5].

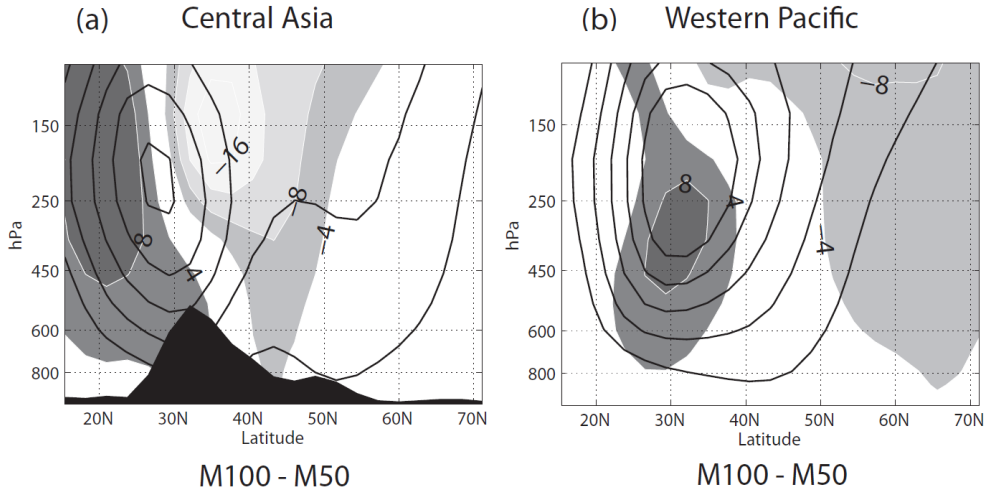

FIG. 2-14: January zonal wind anomalies (shadings) averaged over (a) Central Asia (60E-100E) and (b) East Asia (110E-150E) calculated from the difference between M100 and M50 (M100-M50). Contours are climatological mean, January zonal winds for M50. Contours start from 10 m/s with each interval of 10 m/s.

The latitude-vertical cross section of zonal wind over the Central Asia is shown in Figure 2-14a. The Central Asian mountains strengthen the westerlies at the equatorward flank of the jet (15N-25N) but weaken them at the poleward flank of jet (30N-55N), indicating an equatorward shift of the mean jet. A similar dipole pattern is also found over the Western Pacific (110E-150E) although over this region the anomalies act to strengthen the existing jet, and restrict its poleward extent (Figure 2-14b). It is noteworthy that there is little difference in the anomalous zonal wind structure among M100-M75, M100-M50 and M100-M20 (now shown), indicating that the

[5] The equatorward confinement of baroclinicity is not well detected in the zonal-mean, annual-mean configuration (Figure 1-3a). As the annual-mean baroclinicity is mid-latitudes are much weaker than that of subtropics in boreal winter, the changes in the mid-latitude baroclinicity are not well detected visually unless anomalies are explicitly calculated.

overall equatoward confinement is mostly explained by the Altai-Sayan mountains, not by the Tibetan Plateau.

Does the equatoward shift or confinement of zonal winds over Central Asia suppress the downstream baroclinic instability? Previous studies showed that the meridionally confined narrow jets decreases storminess by horizontal shearing and stretching deformation of the flow in the Pacific (Deng and Mak, 2005). The stronger zonal group velocity relative to the vertical wind shear is also known to weaken the downstream storminess (Harnik and Chang, 2004). Using reanalysis data, Nakamura and Sampe (2002) further found that the years experiencing strong midwinter suppression have meridionally confined zonal wind structure over the Western Pacific and more equatorward refraction of the waveguide.

To address the above questions, we examine the relationship between the North Pacific storminess and the meridional confinement of zonal winds driven by the Central Asian mountains. The degree of zonal wind confinement is measured by calculating the difference of zonal wind speed between the latitude of jet core (28N~33N) and the latitude of 45N (hereafter the 'westerly index'). The choice of 45N is subjective, but our results using this index are insensitive to the choice of the latitude (between 40N-55N). As the zonal wind structure over the Central-Eastern North Pacific (180E-140W) is not much affected by the mountains, we focus on the upstream winds averaged over 110E-150E. A larger westerly index denotes stronger meridional confinement of jet, and stronger barotropic wind shear.

Figure 2-15 shows the sensitivity of the westerly index to the mountains in the upper-troposphere (200-400 hPa mean) and in the lower-troposphere (750-850 hPa mean) separately. The Altai-Sayan mountains effectively confine zonal winds equatorward (see the difference between M100 and M75), whereas decreasing the height of the Tibetan Plateau in addition (M50 and M20) hardly affected the zonal wind structure. On the other hand, North Pacific storminess increase as the mountain is progressively reduced. We infer from this that the barotropic governer effect does not appear to be a dominant factor in explaining our results.

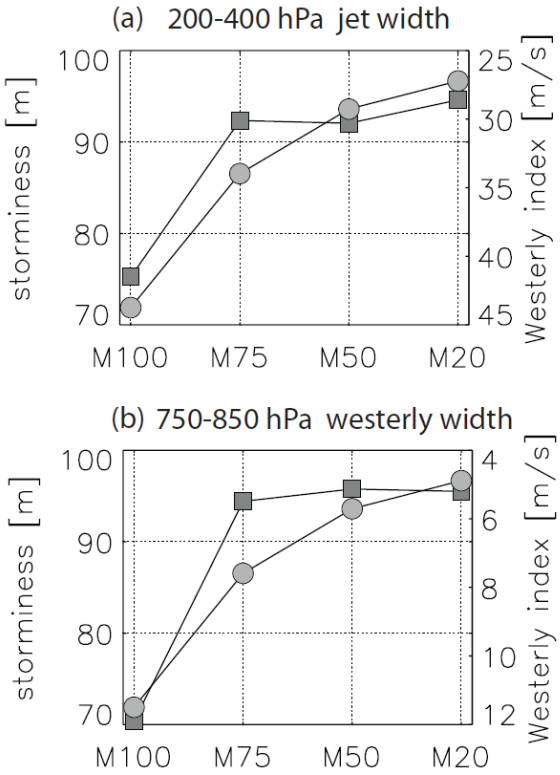

FIG. 2-15: Sensitivities of the westerly index over East Asia (110E-150E) in the (a) upper-troposphere and the (b) lower-troposphere to the varying Central Asian mountains. Larger (smaller) westerly index implies meridionally wide (broad) zonal wind structure. The North Pacific, area-averaged (45N-65N and 140E-220E) storminess are plotted as circles for comparison.

2.6.2. Role of gravity wave drag

Topographically-induced gravity waves play an important role for the upper-troposphere zonal momentum balance (e.g., Shaw et al. 2009). This raises the possibility that the substantial recovery of wintertime storminess in the M50 and M20 experiments (Figures 2-1c and 2-1d) might be in part associated with the weakened gravity wave drag. To isolate the role of the gravity wave drag associated with the sub-grid variability of the Central Asian mountains, we conducted an additional series of experiments where the sub-grid scale variation in the Central Asian mountains was reduced in the same way as for the M75, M50, and M20 experiments, but the height of the mountains were kept to present-day. Hereafter, we label the simulations as G75, G50, and G20, respectively.

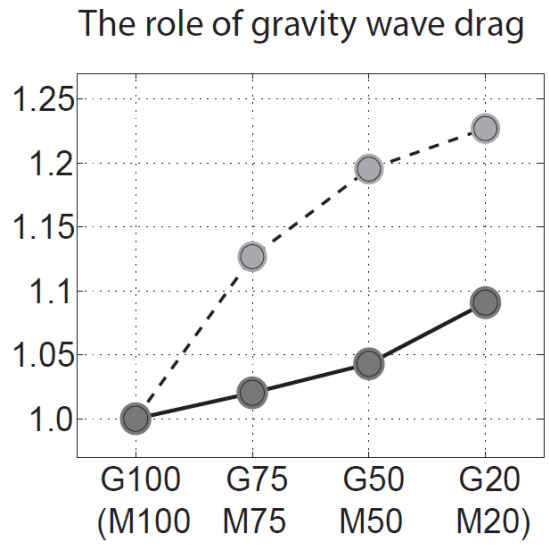

FIG. 2-16: Sensitivities of mid-latitude (32N-67N mean), zonal-mean fractional changes of 300 hPa storminess to the varying sub-grid variability of mountains (G-series experiments; circle with solid lines) and to the varying height plus sub-grid variability of mountains (M-series experiments: circle with dotted lines).

Figure 2-16 shows the sensitivity of storminess to different magnitudes of gravity wave drag (G75, G50, G20) over the Central Asian mountains; by comparison, the corresponding M75, M50, and M20 results are also plotted. The difference between the G75 (G50, G20) and M75 (M50, M20) results thus indicate the non-gravity wave drag contribution to the change in storminess. The zonal-mean storminess increases only by 4.5% if the gravity wave drag is removed over the Altai-Sayan mountains (the G75 experiment) and the Northern Tibetan Plateau regions (the G50 experiment); the contribution increases to around 9% if gravity-wave drag was removed from the rest of the Tibetan Plateau (G20). By comparison, the increase in storminess in the M-series experiments is considerably larger than the G-series; for example, the M50 experiment shows a 19% increase in storminess, compared to 4.5% for the G50 experiment. These results indicate that while the magnitude of gravity-wave drag contributes to the change in storminess, the pure topographic effect of the height of the Central Asian mountains play a larger role. We note that the response of the troposphere circulation to gravity wave drag is dependent on the model resolution (Shaw et al. 2009). We have used relatively coarse model with T42 resolution and 18 vertical levels; it is possible that with vertical resolution in the upper troposphere and the lower stratosphere, quantitatively different results could be found.

2.7. Summary and discussion

In this study, the role of Central Asian mountains on the downstream storminess has been examined by varying the area and height of the Central Asian mountains in NCAR CCM3. We found that the midwinter suppression of the North Pacific storminess almost disappears when the Central Asian mountains are removed. Interestingly, it is the Altai-Sayan mountains, located to the north of the Central Asian mountains, that turns out to be most effective in reducing BCC and downstream storminess. The height of the Altai-Sayan mountains is significantly lower than the Tibetan Plateau, and the zonal winds impinging on the Altai-Sayan mountains is weaker than that impinging on the Tibetan Plateau. Nevertheless, the Altai-Sayan mountains effectively enhance the amplitude of North Pacific stationary waves, and confine the zonal winds equatorward.

We suggest two plausible mechanisms for how the Central Asian mountains suppress storminess in midwinter: (1) by decreasing BCC, especially over the Eastern Eurasian continent, and (2) by reducing downstream eddy development, through changing North Pacific stationary waves that alter the zonal progression of wave packets. The combined effects of the two mechanisms effectively reduce the wintertime North Pacific storminess, even though the low-level baroclinicity has its maximum in winter.

We further examined whether a barotropic governor effect could explain the decrease in BCC and storminess. The Altai-Sayan mountains confine the zonal winds equatorward, increasing the meridional shear of the zonal westerlies, and possibly contribute to suppressing the BCC through the barotropic governor. However, further removal of the Tibetan Plateau had little effect on the zonal wind structure in the Northwestern Pacific; on the other hand, both the BCC and storminess increase further. This result suggests that the barotropic governor effect may not be a dominant factor in explaning our results.

A limitation of our present study is that surface boundary conditions – specifically SST, but also land surface type - are prescribed to present-day, and do not interact with the topography-induced climate changes. SST, and thus atmospheric convection, are potentially sensitive to changes in large-scale mountains. Kitoh (2007) showed in a coupled model study that the global SST and precipitation field changed as the global mountains were uniformly reduced. Changes to the diabatic heating field significantly affect atmospheric circulation and atmospheric available potential energy, and thus potentially changing the upper-level storminess. Our results are thus restricted to the direct effects of the Central Asian mountains on North Pacific storminess; the role of interactive SST in modulating the response will be addressed in the future.

Chapter 3: The impact of the Tibetan Plateau on the onset of the South Asian summer monsoon

Abstract

The role of the Tibetan Plateau on the onset of the South Asian summer monsoon is examined using an atmospheric general circulation model by varying the height and area of the mountains. A series of model integrations shows that the monsoon rainfall increases downstream of the mountains, whereas upstream of the mountains experiences anomalous subsidence. In particular, the Tibetan Plateau triggers low-level cross-equatorial flow and substantial rainfall over the Bay of Bengal during the pre-monsoon season (April-May). While the low-level cross-equatorial flow is established in May, the monsoon's onset over the Arabian Sea and West India is suppressed until early June, probably because of the anomalous subsidence induced by the earlier moist convection over the Bay of Bengal.

Two main causes of the earlier monsoon rainfall over the Bay of Bengal are suggested. First, the response of stationary waves to the orographic forcing, such as low-level cyclonic motions, seems to trigger the earlier rainfall over the Bay of Bengal. Because low-level westerlies exist over the Southern Tibetan Plateau during pre-monsoon season, the stationary wave response to the mountains is likely to occur. Second, the Tibetan Plateau blocks cold-dry air advection from the extratropics, which contributes to maintaining higher subcloud layer entropy over the subcontinent of India.

3.1. Introduction

Many Atmospheric General Circulations Models (AGCMs) consistently simulate stronger South Asian summer monsoon circulation in the presence of the Tibetan Plateau (Hahn and Manabe 1975; Kutzbach et al. 1989; Yasunari et al. 2006; Boos and Kuang 2009). Intense research has been done to understand why the monsoon circulation is enhanced by the Tibetan Plateau. A few works interpret the upper-level (convective) latent heating as a heat source for driving the monsoon circulation (e.g. Webster et al. 1998), but It can be misleading to assume the latent heating as an external forcing for the circulation. Under quasi-equilibrium point of view, the moist convection is strongly constrained by the circulation (Emanual 1994). Many other studies suggest that the surface sensible (latent) heat flux over the Western (Eastern) Tibetan Plateau would be a main heat source, leading to moisture sinks over the South Asia monsoon region (Yanai and Wu 2006; Luo and Yanai 1984). However, the magnitudes of these surface fluxes are not particularly larger than those of other subtropical areas.

A recent modeling study by Boos and Kuang (2009) provides an advanced view on the role of the Tibetan Plateau – as a thermal insulator. As the Tibetan Plateau reduces cold-dry air advection from the extratropics, the subcloud layer entropy over India could be maintained higher than other subtropics. Indeed, the narrow mountains surrounding the Northern India in the numerical simulations of Boos and Kuang (2009) are turned out to effectively strengthen the monsoon rainfall and the low-level winds during the peak monsoon season (July-August). While the 'narrow mountains' in Boos and Kuang (2009) may well represent a thermal insulator during the peak monsoon season, it is still possible that the narrow mountains could have their dynamical effects during pre-monsoon season (April and May) or monsoon's onset (late May and early June) when the low-level westerly winds still exist over the South-Western Tibetan Plateau. In many cases, mountains in mid-latitudes refract waves south-eastward and generate low-level cyclonic motions over downstream of the mountains, which is named as linear response of stationary waves to orographic forcing (Held et al. 2002; Cook and Held 1992).

In this study, possible dynamical effects of the Tibetan Plateau on monsoon rainfall will be explored by varying the height and area of the mountains in a comprehensive AGCM. The response of rainfall and low-level winds during pre-monsoon season will be particularly emphasized. There are two important reasons that we focus on the pre-monsoon process. First, it is easier to define the dynamical effect of the mountains. As the westerly wind speeds over the South-Western Tibetan Plateau are maintained around 3~8 m/s at 700-800 hPa in April and May, the linearized isentropic equation (Cook and Held 1992) is likely to be applicable. Second, it is more likely to see clear responses in the meridional direction of low-level cross-equatorial flow. Once the monsoon is in mature phase, the direction of the northward cross-equatorial winds may not be well affected by external perturbations. The low-level cross-equatorial winds start to develop in mid-April and gradually progress northward in May (Boos 2008). If the Tibetan Plateau can provide dynamic or thermodynamic source of convective instability, the resulting moist convection and the subsequent wind-evaporation feedback may substantially affect the seasonal development of low-level cross-equatorial flow.

3.2. Model and simulated monsoon

3.2.1. Data and model

The Medium Range Weather Forecasts 40 year Reanalysis (ECMWF ERA-40; Uppala et al. 2005) is used for the evolution of low-level monsoonal winds. In particular, we use the version of ERA-40 produced by NCAR's Data Support Section (**http://www.cgd.ucar.edu/cas/catalog/ecmwf/era40)** consisting of monthly means for 256x128 regular Gaussian grids at T-85 spectral truncation and 23 pressure levels spanning September 1957 to August 2002. For monsoon precipitation, the Climate Prediction Center (CPC) Merged Analysis of Precipitation (CMAP; Xie and Arkin 1997) data set was used. The CMAP data consist of monthly means at a horizontal resolution of 2.5° x 2.5° spanning January 1979 to December 2005.

To understand the role of the Tibetan Plateau on the onset of the South Asian summer monsoon, a set of AGCM experiments have been conducted. We used the Community Climate Model 3.10 (CCM3; Kiehl et al. 1998) at T42 horizontal resolution and the standard 18 levels in the vertical. Monthly-varying climatological surface boundary conditions such as land surface type, sea surface temperatures (SSTs) and sea ice, are prescribed in the model. The climatological monthly mean SSTs are calculated from the 40 years' monthly mean Reynolds optimum interpolation data (Reynolds et al. 2002), spanning from 1960 to 2000.

In all model integrations, the same boundary conditions are used except for topography over South and Central Asia. The 'full-Tibet' experiment is the control experiment, maintaining all the mountains at present-day heights (contours in Figures 3-1c, 3-1d). Following the idea of Boos and Kuang (2009), we also designed a 'narrow-Tibet' experiment. It is not only because it could be useful to identify the thermal insulator effect (Boos and Kuang, 2009), but also to check if the typical stationary wave response to a topography can occur over the 'narrow-Tibet'. In the narrow-Tibet experiment, the entire Tibetan Plateau area is further reduced by 95%, retaining only the southern part of the Tibetan Plateau (contours in Figure 3-2a). Finally, in the 'no-Tibet' experiment, the entire Tibetan Plateau including the Himalaya is removed by 95%. It should be noted that the imposed sub-grid variability of the mountain height, which is used for the gravity wave drag parameterization, has also been reduced with mountain height (so by 95% if the mountain height is reduced by 95%). These experiments are summarized in Table 3-1.

Each experiment ran for 27 years, and last 23 years are used for the analysis. As climatological monthly-mean SSTs are prescribed, 4 years of integration was sufficient for spin-up.

Table 3-1. AGCM design of experiments

Experiments	Descriptions	Topography boundaries
Full-Tibet	Control experiment with full topography	contours in Figures 3-1c, 3-1d
Narrow-Tibet	Altai-Sayan mountains (42N-55N; 55E-120E) and the most part of the Tibetan Plateau (22N-42N; 55E-120E) are reduced by 95% except the Himalaya and the mountains over Northern India.	contours in Figure 3-2a
No-Tibet	Altai-Sayan mountains and the entire Tibetan Plateau are reduced by 95%	contours in Figures 3-2b

3.2.2. Simulated South Asian summer monsoon

A revised convective parameterization closure (Zhang and Mu 2005, hereafter ZM05) based on the Zhang-McFarlane scheme was implemented. Under the ZM05 scheme, convective closure consists of large-scale forcing of temperature and humidity in the free troposphere rather than convective available potential energy as in the original scheme. The revised convection scheme is superior to the standard CCM3 convection scheme (Zhang and McFarlane 1995) in simulating the Indo-Pacific tropical climate: in particular, the ZM05 scheme strengthens low-level winds and increases monsoon precipitation over the Western Pacific, thereby alleviating the negative precipitation bias seen in the original convection scheme by Zhang and McFarlane (1995); it also removes the spurious heavy precipitation over the Arabian Peninsula and the Western Indian Ocean simulated by the original convection scheme.

However, monsoon rainfall simulated by CCM3 with the convection scheme by ZM05 (Figure 3-1c) still has several important deficiencies when compared to observations (Figure 3-1a). In particular, low-level westerlies over the North Indian Ocean are stronger than ERA-40 by 50-60% and the precipitation over West India and the Bay of Bengal are substantially larger than the CMAP. Evaporation from the North Indian Ocean is about 30-40% larger than the one in ERA-40, which is consistent with the stronger surface westerlies found in the model. While the model over-estimates the South Asian summer monsoon rainfall, the rainfall over the equatorial Indian Ocean is substantially underestimated. Similar biases occur when a slab ocean is coupled to our CCM3 configuration.

3.3. Response of low-level winds and rainfall to the Tibetan Plateau

The monsoon's onset is typically defined by the heavy rainfall over the west coast of India, which often starts abruptly in early June, but the low-level cross-equatorial winds (i.e., Somali

jet) undergoes a gradual development by season. The northward cross-equatorial flow typically starts in April over the off-equatorial South-Western Indian Ocean, and then it shifts westward in May to become zonally concentrated near the East African highlands (Boos 2008). Insolation would be the foundamental source for the seasonal evolution of winds and rainfall. It is less understood if the Tibetan Plateau can provide additional source of convective instability, which can accelerate the northward progression of the cross-equatorial flow. In this chapter, the possible role of the Tibetan Plateau on the monsoon progression is tested by varying the height and area of the Tibetan Plateau. The response of low-level winds and rainfall to the orographic forcing during pre-monsoon season (April and May) is presented in section 3.3.1. The seasonal evolution of convective heating over the Western Indian Ocean is investigated in section 3.3.2.

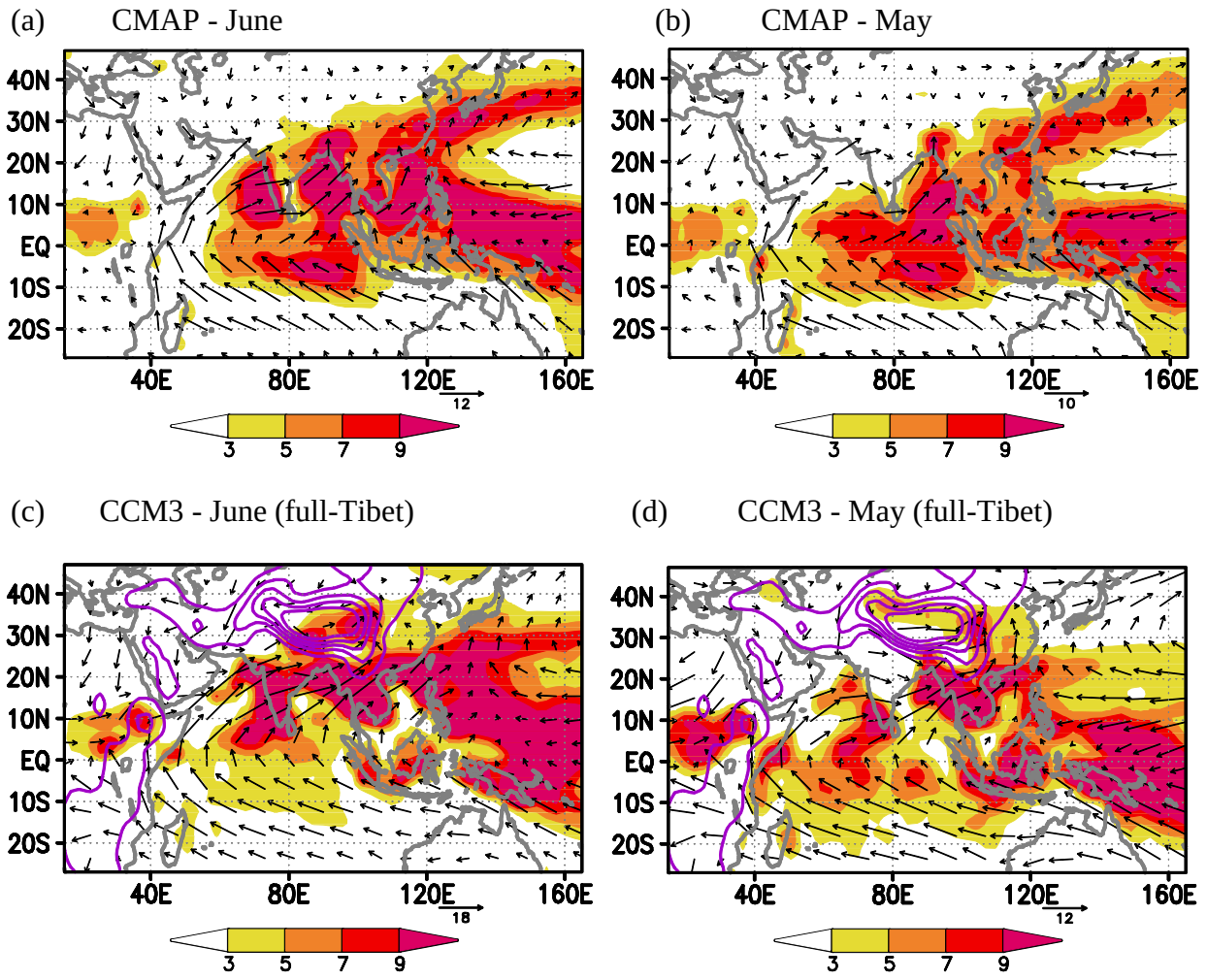

FIG. 3-1: CMAP precipitation (shadings: mm day^{-1}) and ERA-40 winds at 900 hPa (vectors: m s^{-1}) for (a) June and (b) May. (c) and (d) are same as (a) and (b) except for CCM3 simulated precipitation and 900 hPa winds. Contours indicate mountain height, starting from 800 m with each contour interval of 800 m.

(a) CCM3 - May (narrow-Tibet) (b) CCM3 - May (no-Tibet)

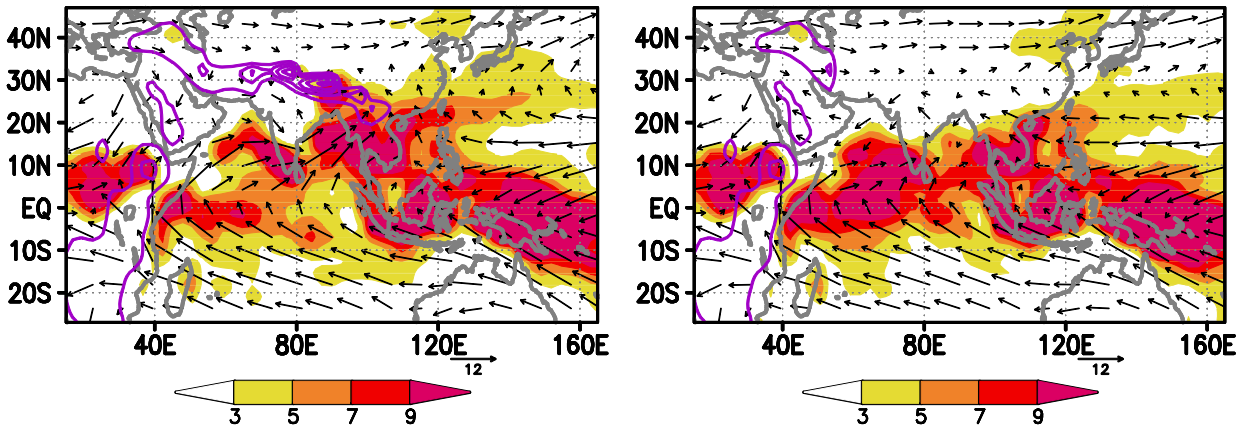

FIG. 3-2: Simulated precipitation (shadings: mm day^{-1}) and 900 hPa winds (vectors: m s^{-1}) in May for the (a) narrow-Tibet and for the (b) no-Tibet experiments. Contours indicate mountain height, starting from 800 m with each contour interval of 800 m.

3.3.1. Tibetan Plateau and zonally asymmetric rainfall pattern

The CMAP rainfall over the tropical Indian Ocean exhibits zonally asymmetric pattern in May, with much higher rainfall over the Eastern Indian Ocean (e.g. Bay of Bengal) than the Western Indian Ocean (e.g. Arabian Sea; Figure 3-1b). The low-level cross-equatorial flow is already set up, although the Somali jet speed at 900 hPa is around 5~6 m/s (Figure 3-1b), which is about half of the speed in June. The overall low-level wind pattern in May looks quite similar to the ones in June, but the rainfall over the off-equatorial North Indian Ocean, especially over the Arabian Sea and West India is much weaker than in June (compare Figure 3-1a and 3-1b). CCM3 simulated rainfall pattern in May (Figure 3-1d) doesn't match well with CMAP, but it has some nontrivial advantages. In particular, simulated rainfall in May exhibits zonally asymmetric pattern, with obvious preference over the Bay of Bengal than the Arabian Sea, which is consistent with CMAP. Also, simulated Somali jet and low-level wind pattern over the Bay of Bengal look qualitatively consistent with the ones in ERA40.

The low-level winds and the rainfall pattern are well reproduced by the narrow-Tibet experiment (Figure 3-2a), verifying that Southern Tibetan Plateau would be a sufficient boundary condition for strengthening the monsoon cross-equatorial flow (Boos and Kuang 2009). The zonally asymmetric rainfall pattern and the strong Somali jet disappear in the case when the Tibetan Plateau is removed (Figure 3-2b). Rainfall over the Bay of Bengal decreases a lot, whereas rainfall over the Western Indian Ocean increases, leading to zonally symmetric and well organized ITCZ near the equator. It is probably because the anomalous subsidence effect on the Western Indian Ocean disappears as the moist convection over the Bay of Bengal substantially reduces. The reduced moist convection over the Bay of Bengal is accompanied by the weakening (or disappearance) of the Somali jet, suggesting that the low-level convergence over the Bay of Bengal can affect the large-scale monsoonal flow.

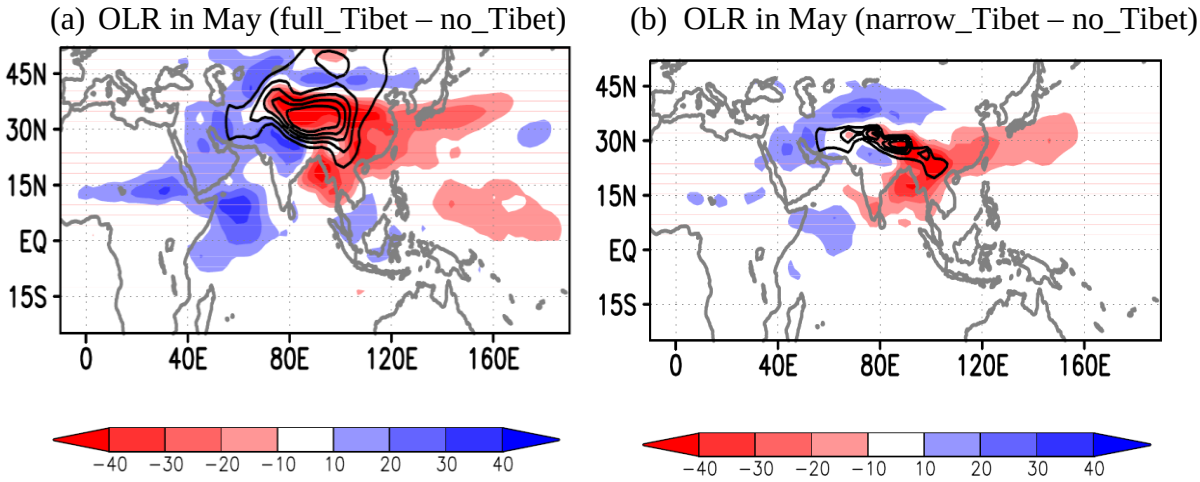

FIG. 3-3: Simulated anomalous OLR (shadings: W m^{-2}) calculated from the differences between the (a) full-Tibet and no-Tibet (full-Tibet minus no-Tibet), and between the (a) narrow-Tibet and no-Tibet (narrow-Tibet minus no-Tibet). Contours indicate mountain height, starting from 800 m with each contour interval of 800 m.

The zonally asymmetric rainfall pattern is consistently simulated by CCM3 in April with the full Tibetan Plateau (not shown). The major difference between April and May is the presence of the low-level cross equatorial winds. Unlike in May, the moist convection over the Bay of Bengal is not accompanied by the large-scale cross-equatorial flow, but localized low-level south-westerlies develop (not shown). Similar to the case in May, the zonally asymmetric rainfall pattern disappears and the ITCZ gets meridionally concentrated without the Tibetan Plateau in April (not shown).

The preference of rainfall over downstream of the mountains can be seen more clearly in the anomalous Outgoing Longwave Radiation (OLR). In May, the full Tibetan Plateau reduces OLR by 10-20% over wide downstream of the mountains compared to the case when there is no Tibetan Plateau (Figure 3-3a). The reduced OLR over downstream of the mountain is accompanied by increased OLR over upstream of the mountain, approximately within the Rossby radius of deformation (e.g. Pakistan, Afghanistan and Western Indian Ocean). Interestingly, the anomalous subsidence (i.e., increased OLR) and anomalous low-level equatorward flow (now shown) occur over Central Africa, located beyond the Rossby radius of deformation. Considering that $f << N$ can be applied to Earth's many subtropical regions, the Sverdrup's vorticity balance, $\beta v \approx f \frac{\partial \omega}{\partial p}$ is likely to be applicable to explain the anomalous low-level equatorward flow over Central Africa.

Similar downstream preference of rainfall and the anomalous subsidence over upstream consistently occur only in the presence of the narrow-Tibet (Figure 3-3b). Unlike the full-Tibet case, the areal contrast of OLR is smaller and the anomalous subsidence over Central Africa is much weaker. Considering that the monsoon strength between the full-Tibet and the narrow-Tibet are comparable each other (compare Figure 3-1d and Figure 3-2a, or compare Figure 3-4a and 3-4b), the large-scale subsidence doesn't seem to be always dependent on the local

convective strength. Instead, the altered diabatic heating field (e.g. stronger convective heating in the Bay of Bengal) interacting with the topography boundary conditions seems to explain the stronger subsidence over wider upstream of the mountains. The role of a mountain for driving localized subsidence over upstream of the mountain for a specified off-equatorial diabatic heating was found by Rodwell and Hoskins (2001). Our speculation is a little different from the Rodwell-Hoskins mechanism as we hypothesize that the mountains can strengthen the subsidence over longitudinally wider upstream areas.

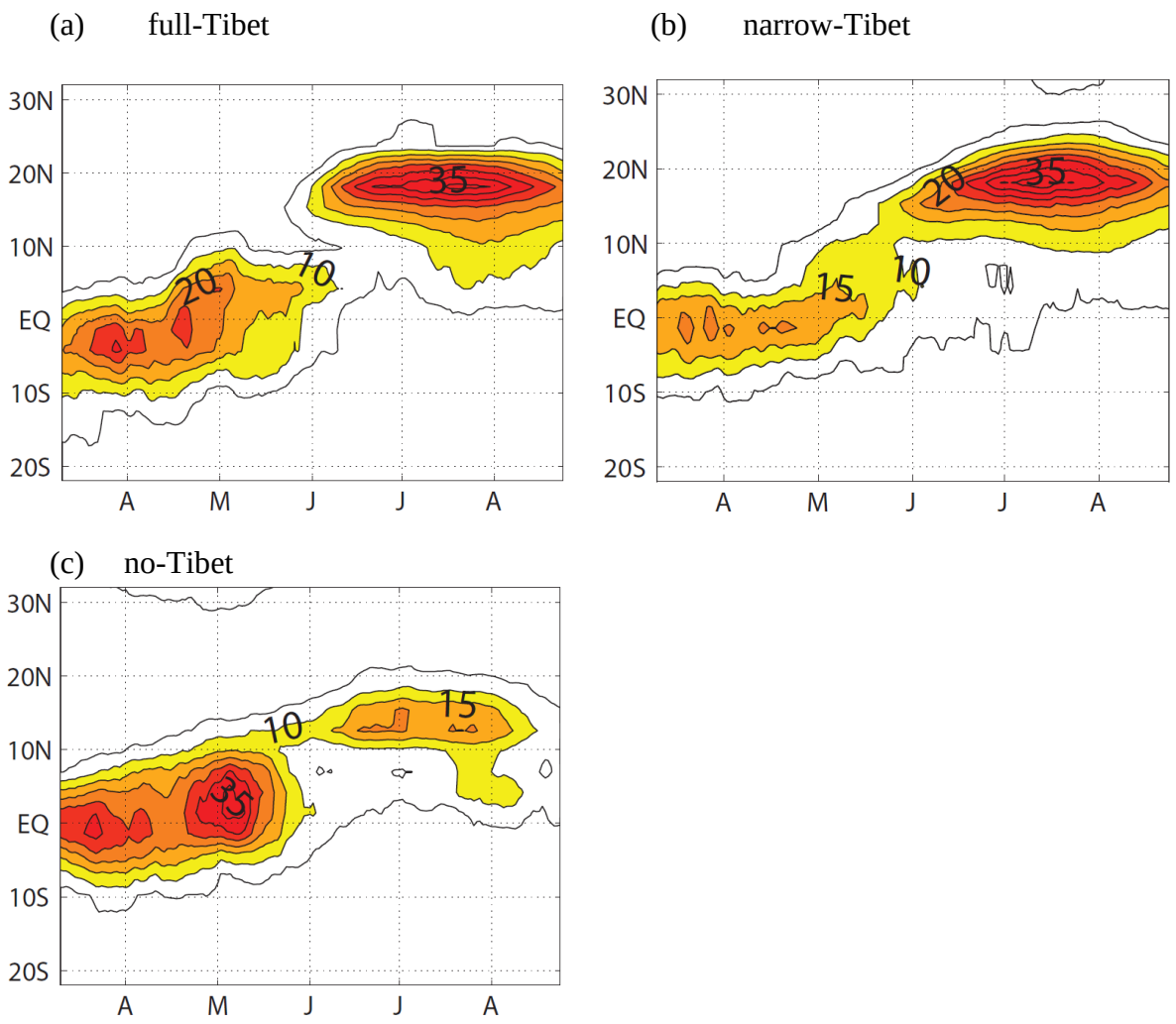

FIG. 3-4: Seasonal evolution of the simulated upper-troposphere convective heating (150-400 hPa; W m^{-2}) over the Western Indian Ocean and the subcontinent of India (55E-80E mean) for the (a) full-Tibet, (b) narrow-Tibet, and for the (b) no-Tibet experiments. Contours start from 5 W m^{-2} with each contour interval of 5 W m^{-2}. Values higher than 10 W m^{-2} are shaded. Each tick at the bottom indicates every 15th day of each month.

3.3.2. Delayed monsoon's onset over West India

As identified both in ERA-40 and CCM3, the low-level cross-equatorial winds set up in May, which is earlier than the actual onset of monsoon rainfall over the Arabian Sea and the West India. What causes such a delay in the monsoon rainfall even though low-level monsoonal winds are already substantial in May?

The seasonal evolution of the upper-troposphere convective heating (150-400 hPa) averaged over the Western Indian Ocean and the West India (55E-80E zonal mean) indicates abrupt northward shift of the deep convection zone (Figure 3-4a). The deep convection is confined near the equator until much stronger deep convection is suddenly developed over the off-equatorial monsoon region (17N-22N) in early-mid June. The similar abrupt onset of deep convection is simulated by the narrow-Tibet experiment (Figure 3-4b). On the other hand, the removal of the Tibetan Plateau simulates smoother monsoon transition, with relatively gradual northward shift of the deep convection zone (Figure 3-4c). Also, the deep convection near the equator before monsoon's onset gets much stronger than the one with the Tibetan Plateau or with the narrow-Tibet. It is probably because the substantial moist convection over the Bay of Bengal suppresses the low-level convergence over the Arabian Sea until early June, which is consistent with the anomalous OLR (Figure 3-3). This anomalous subsidence effect might in part be able to explain the delayed onset of monsoon rainfall over West India, which doesn't start by early June.

During the peak monsoon season (July-Aug), there is a substantial difference in the magnitude of deep convection between the experiments with and without the Tibetan Plateau. In the presence of the Tibetan Plateau or narrow-Tibet, the upper-troposphere convective heating gets stronger by 100% compared to the one without the Tibetan Plateau. The stronger deep convection is accompanied by slightly northward position of deep convection zone. In the presence of the Tibetan Plateau, the maximum deep convection occurs around 16~18N, whereas it shifts down to 12~14N without the Tibetan Plateau. In the zonally-asymmetric real atmosphere, it can be challenging to verify if the slightly poleward displacement of the monsoon circulation manifests a further shift to the angular-momentum conserving regime (Bordoni and Schneider 2008).

3.4. Possible mechanisms

Why would the Tibetan Plateau substantially strengthen the moist convection over the Bay of Bengal during the pre-monsoon season, in April and May? Is there an external source for the convective instability? As Boos and Kuang (2009) suggest, the Tibetan Plateau may have played a role as a thermal insulator by blocking the cold and dry air advection from the South Asian continent in April and May. The thermal insulator effect may be particularly efficient in boreal spring when the meridional gradient of the low-level Moist Static Energy (MSE) is much larger than in the boreal summer. However, the strong low-level westerlies over on the Southern Tibetan Plateau in April and May cast more challenges, such as topography-forced stationary waves and barotropic wind shear.

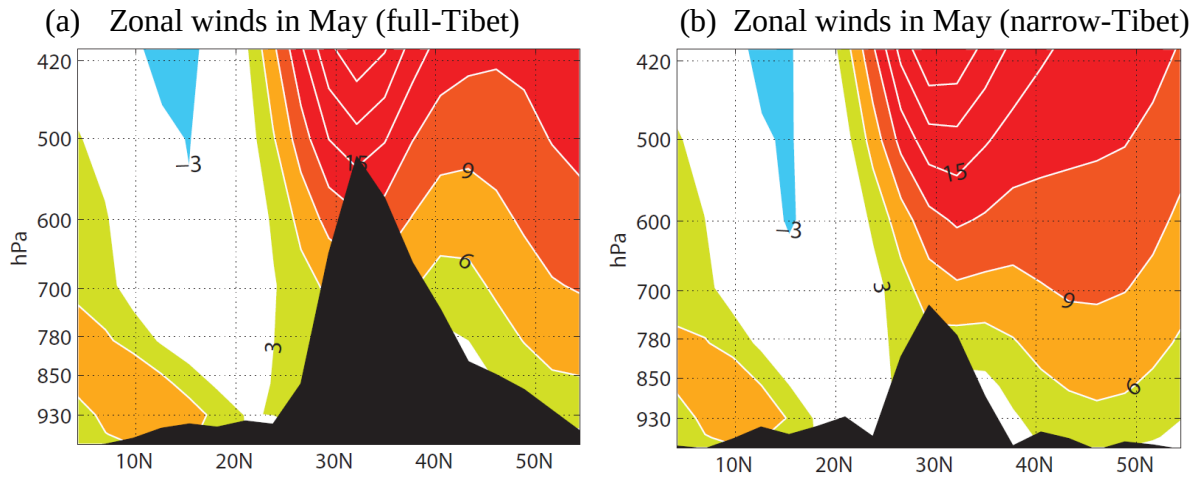

FIG. 3-5: Zonal wind averaged over the longitudinal interval of 45E to 90E for the (a) full-Tibet and for the (b) narrow-Tibet experiments. Black shadings indicate mountain profiles over the longitudinal interval of 45E and 90E. Contour interval is 3 m s^{-1}, and the values between -3 and 3 m s^{-1} are not shaded.

3.4.1. Dynamical effect of the Tibetan Plateau

Zonal winds and mountain profiles in May over western section of the South Asian monsoon region (45E-90E) are displayed for the full-Tibet (Figure 3-5a) and for the narrow-Tibet (Figure 3-5b) experiments. In both cases, strong subtropical jets still hang over the Southern Tibetan Plateau, suggesting that the meridional temperature gradient over the Northern India is still strong in May, not alone in April. The meridional temperature gradient would be strongest at the edge of the Hadley Cell, where subtropical jets develop out of thermal wind balance (Vallis and Gerber 2008). The low-level westerly impinging on the Southern Tibetan Plateau casts a possibility that the theory of northern winter stationary waves might be applicable to the northern summer (Held et al. 2002).

Intense research has been done to understand the role of the large-scale mountains on altering the stationary waves (e.g. Held et al. 2002; Cook and Held 1992). Cook and Held (1992) suggest a linearized potential temperature equation with a simplified representation of vertical motion over a mountain to explain the response of stationary waves to a mountain:

$$w = v \cdot \nabla h \approx \frac{\bar{U}}{a\cos\phi}\frac{\partial h}{\partial \lambda} \qquad (3.1)$$

$$\frac{\bar{U}}{a\cos\phi}\frac{\partial \Theta'}{\partial \lambda} + \frac{v'}{a\cos\phi}\frac{\partial \bar{\Theta}}{\partial \phi} = -w\frac{\partial \bar{\Theta}}{\partial z} \qquad (3.2)$$

Equation (3.1) represents the near-surface vertical motion over a mountain approximated by westerly wind over a mountain slope. Equation (3.2) represents a linearized, near-surface potential temperature conservation equation. If the meridional temperature gradient is substantially larger over the Southern Tibetan Plateau, which would be particularly true in boreal winter, the second term of the equation (3.2) would be dominant over the first term. And then, the typical linear response of stationary waves to a mountain, such as the near-surface cyclonic motions over downstream, where $\frac{\partial h}{\partial \lambda} < 0$, is likely to occur. The linear response is also accompanied by the south-eastward propagation of wave packets over the mountain. A nonlinear response can occur is the first term gets comparable to the second term of the equation (3.2). In that case, the near-surface cyclonic motions would occur right over the mountain (Cook and Held 1992).

We hypothesize that these mountain-induced near-surface cyclonic motions in downstream of the mountain (i.e. linear response) or over the mountain (i.e. nonlinear response) could be a potential source for the convective instability during the pre-monsoon season. Separating the mountain's dynamical effect from the thermal insulator effect (Boos and Kuang 2009) on monsoon rainfall would be a challenging problem, especially in a comprehensive AGCM. For example, the mountain-induced moist convection over the Bay of Bengal would be accompanied by an instantaneous response of low-level winds and surface evaporation, which might disturb the signal of cyclonic motions. Changing the height of the mountains may not be an elegant solution for this problem as both the thermal insulator effect and the stationary waves would be dependent on the height of the mountains[6]. The best alternate way to identify the effect from the barotropic wind shear would be using a linear dry model, where all kinds of complicated feedbacks associated with the moist convection are excluded.

3.4.2. Thermal insulator effect of the Tibetan Plateau

The role of the Tibetan Plateau as a thermal insulator has been nicely verified by Boos and Kuang (2009). In the model of Boos and Kuang (2009), the low-level cross-equatorial winds and monsoon rainfall get substantially weaker without the Tibetan Plateau during the peak monsoon season (June-July). Similar weakening of low-level winds and substantial reduction of rainfall during the peak monsoon season consistently occurs without the Tibetan Plateau in our CCM3 configurations (not shown).

The subtropical ventilation, inferred from the MSE advection, has been suggested as a key factor for inhibiting the northward progression of monsoon rainfall (Chou and Neelin 2003). We try to explicitly measure the thermal insulator effect by calculating the low-level MSE advection. However, the method we use, i.e., simple calculation of MSE advection from the model outputs, is fundamentally different from the method used by Chou and Neelin (2003), where the MSE advection can actively affect the MSE budget in every model time step. We caution that it can be potentially problematic to interpret the negative MSE advection calculated from the model

[6] We caveat that the mountain height is not always an essential ingredient for amplifying the stationary waves (Held et al. 2002).

outputs as ventilation reducing the convective available potential energy. The MSE advection could be just a balancing budget associated with the low-level MSE convergence.

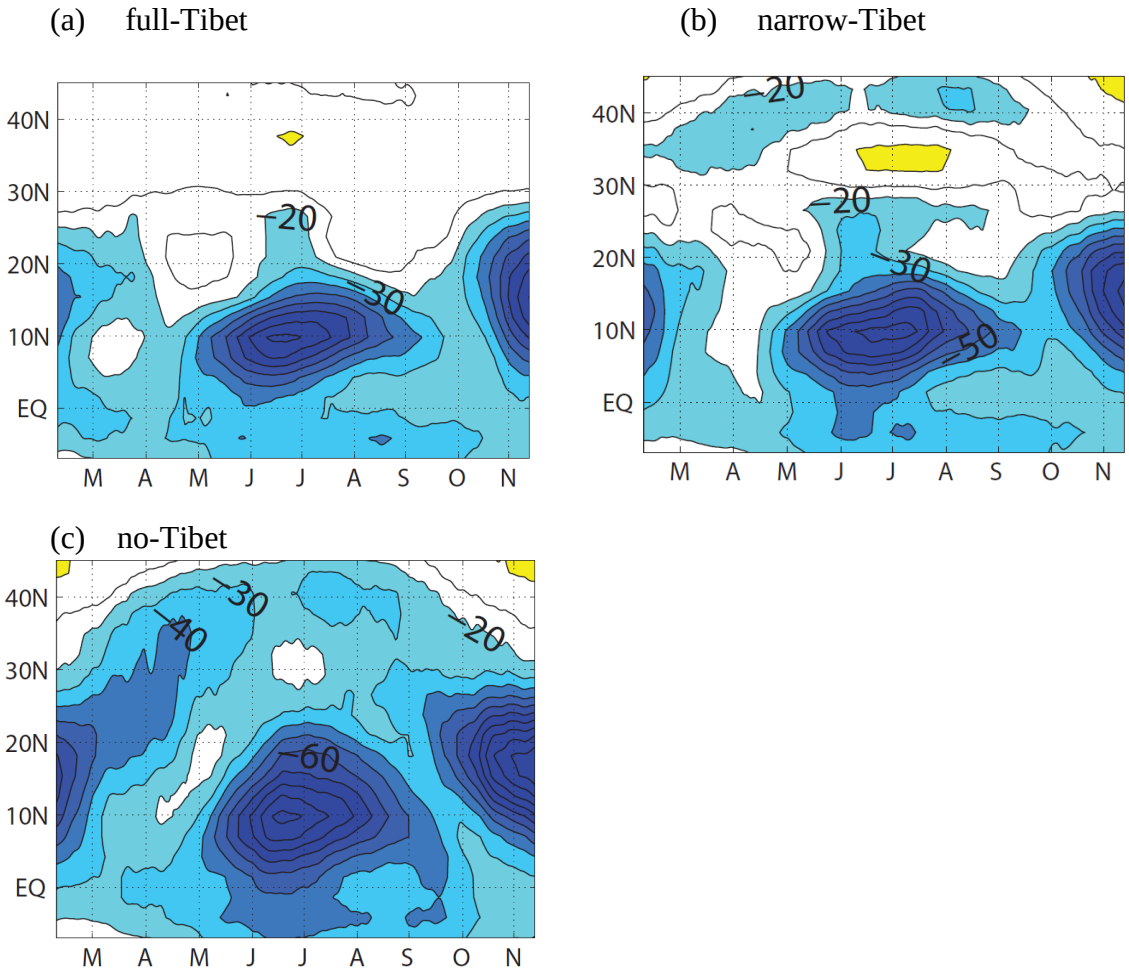

FIG. 3-6: Seasonal evolution of lower-troposphere MSE advection (850-1000 hPa; W m^{-2}) over the North Indian Ocean and the subcontinent of India (50E-100E mean) for the (a) full-Tibet, (b) narrow-Tibet, and the (b) no-Tibet experiments. Each tick at the bottom indicates every 15th day of each month.

Following Chou and Neelin (2003), ventilation can be defined by the horizontal MSE advection, $<-v\cdot\nabla(q+T)>$, where v represents horizontal winds, and q and T represent the specific humidity and temperature respectively. Both q and T are converted by energy unit by multiplying the latent heat of vaporization, L_v and the specific heat capacity, C_p respectively. Bracket represents vertical integration from the surface to 850 hPa. The low-level MSE

advection is mostly negative (i.e. ventilating) in the tropics as the low-level winds blow into more humid regions where deep convection frequently occurs.

Figure 3-6 shows the seasonal evolution of low-level (850-100 hPa) MSE advection averaged over the South Asian monsoon sector (50E-100E) with different topography boundary conditions. The ventilation would be strongest during the peak monsoon season when the low-level winds are strongest, especially around 10N where Somali jets pass by (Figure 3-6). The biggest differences between the full-Tibet (or narrow-Tibet) and the no-Tibet experiments are in the ventilation over subtropics (20N-35N). Unlike the tropics, the subtropical ventilations are often associated with the cold and dry air (relatively lower MSE) advection by northerly winds. Without the Tibetan Plateau (or narrow-Tibet), the ventilation in the subtropics becomes particularly strong during the pre-monsoon and monsoon's onset (from late April to early June), which may have suppressed the northward progression of monsoon rainfall.

3.5. Summary and future work

Using NCAR CCM3 with climatologically specified SSTs, we demonstrated that the Tibetan Plateau can trigger earlier onset of monsoon rainfall over the Bay of Bengal and low-level cross-equatorial flow. Himalaya-type narrow mountains turn out to be sufficient boundary conditions for strengthening the monsoon circulation, which is consistent with Boos and Kuang (2009). While the thermal insulator effect of the Tibetan Plateau would be a feasible explanation for strengthening the monsoon circulation, we suggest that the topography-forced barotropic wind shear could be another source of convective instability over the Bay of Bengal. Because low-level westerlies still exist during the pre-monsoon season or monsoon's onset, the stationary wave response to a mountain is likely to occur with the 'narrow-Tibet' boundary conditions.

The earlier moist convection over the Bay of Bengal during the pre-monsoon season (April-May) is accompanied by the anomalous subsidence over the Western Indian Ocean, which contributes to suppressing the monsoon's onset over the Arabian Sea and West India by early June. Anomalous OLR field calculated from the differences between with and without Tibetan Plateau exhibits increased rainfall in downstream of the mountains, whereas upstream of the mountains experience anomalous subsidence. We hypothesize that the interaction between the altered diabatic heatings field (i.e. stronger latent heating over the Bay of Bengal) and the topography (i.e. Tibetan Plateau) may strengthen the subsidence in upstream of the mountains.

In summary, our analyses on a full AGCM outputs by various topography boundary conditions cast two challenging questions, which require different hierarchies of AGCM to elucidate:

Question-1: Would the Tibetan Plateau provide low-level cyclonic motions over the Bay of Bengal, which can induce convective instability?

Question-2: How would the convective heating over the Bay of Bengal interact with the Tibetan Plateau? Would it strengthen the subsidence in upstream of the Tibetan Plateau?

Chapter 4: The delayed effect of major El Niño events on Indian monsoon rainfall

Abstract

Previous studies have shown that boreal summer Indian monsoon rainfall is, on average, significantly above normal after major El Niño events. In this study, the underlying causes of this rainfall response are examined using both observational analysis and atmospheric general circulation model (AGCM) simulations. Moist static energy budgets for two strong El Niño events (1982-83 and 1997-98), estimated from monthly ERA-40, suggest that stronger low-level moisture transport and reduced moist stability associated with a warmer North Indian Ocean (NIO) can increase monsoon rainfall, despite a weakened monsoon circulation.

The tradeoff between a dynamically weaker monsoon and moist processes favoring enhanced monsoonal rainfall is broken during the late monsoon season (August-September) as the warm NIO enhances surface latent heat flux and the monsoon circulation relaxes back to the climatological mean. The monsoon circulation strength and the moist processes work together in the late season, which explains the observed tendency for monsoonal rainfall increases during the late monsoon season after strong winter El Niño conditions.

Idealized AGCM experiments with a mixed layer Ocean demonstrate that the remnant but weaker-than-peak warm SSTs in the eastern equatorial Pacific during spring and the early summer following winter El Niños substantially contribute to the NIO warming. Our results suggest that local air-sea interactions in the tropical Indian Ocean after winter El Niño are strongly dependent on the details of El Niño's decaying trend.

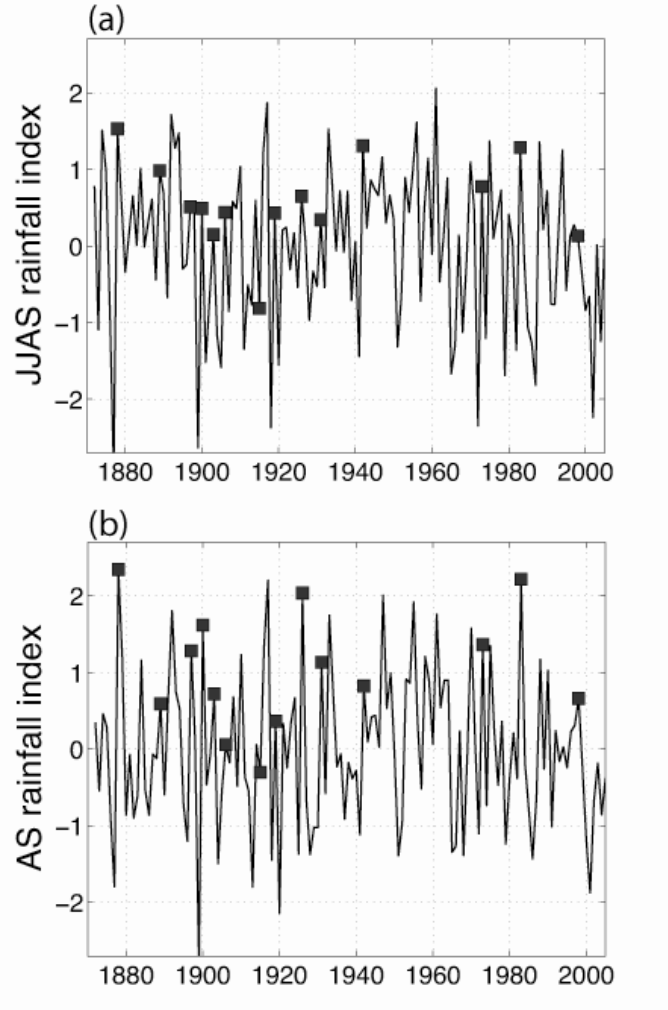

FIG. 4-1: (a) Standardized Jun-Jul-Aug-Sep mean All-Indian monsoon rainfall index (Parthasarathy et al., 1995; solid line) and the years with strong winter El Niños before the summer monsoon season (squares). Strong winter El Niño years are defined as those Nov-Dec-Jan means with a standardized Niño3 value > 1.4. (b) is same as (a), except for late season (Aug-Sep) Indian monsoon rainfall.

4.1. Introduction

While Indian monsoon rainfall is known to be suppressed during the summer preceding peak winter El Niño conditions, a tendency for above normal precipitation during the subsequent summer season has been noted (Shukla 1995; Webster et al. 1998; hereafter we refer to the latter as the "delayed effect"). Considered over the entire monsoon season (Jun-Jul-Aug-Sep, hereafter JJAS), the relationship between a common measure of All-Indian monsoon rainfall and ENSO is statistically

weak (Figure 4-1a). However, looking only at the late monsoon season (Aug-Sep, AS)[1] indicates a more robust delayed effect (Figure 4-1b): approximately half of the AS periods following strong winter El Niños experience positive rainfall anomalies exceeding one standard deviation.

The delayed effect is often explained in terms of the development of La Niña phase conditions subsequent to strong El Niño events (Shukla 1995). Since the developing La Niña signal is generally stronger in AS relative to JJ, the contemporaneous effect of developing La Niña conditions may contribute to above normal rainfall in AS. However, absent in this view is the potential role of residual Indian Ocean warming induced by winter El Niño conditions, i.e., the upper ocean's thermal memory of strong El Niño events.

The seasonal evolution of El Niño-related air-sea interactions in the Indo-Western tropical Pacific Ocean has been extensively investigated. Xie et al. (2002) showed that El Nino-induced westward-propagating oceanic Rossby waves can warm the southwest Indian Ocean. Such warming may be amplified by anomalous anticyclonic surface winds associated with higher surface pressures over the south equatorial Indian Ocean, which lead to deeper thermoclines (Huang and Shukla 2005). Tropospheric warming has also been suggested as another mechanism for the basin-wide tropical Indian Ocean warming (Chiang and Lintner 2005), especially in the spring season following major winter El Niño events. The basin-wide tropical Indian Ocean warming in boreal spring does not decay immediately but may persist well into the summer (active monsoon) season. Although ocean dynamics may contribute to the persistence of Indian Ocean SSTs (Webster et al. 1999), simulations of AGCMs coupled to ocean mixed layer models (e.g., Lau et al. 2005) suggest significant persistence simply from thermodynamic surface flux controls.

A few recent studies have noted the influence of locally warm SSTs on Indian monsoon rainfall. For example, Terray et al. (2003) suggested that the anomalously warm SIO SSTs in boreal spring slowly transition to warm NIO SSTs and strengthen the local Hadley circulation near India and intensify Indian monsoon rainfall during the late monsoon season (AS). On the other hand, Annamalai et al. (2005) found that persistent SIO warming delays Indian summer monsoon onset by a week. In this paper, we provide a comprehensive mechanism for the increasing Indian monsoon rainfall by examining two major El Niño events, 1982-83 and 1997-98, which are the strongest 20th century El Niño events for which extensive satellite data coverage exists. In our analysis, we focus on the spatial and temporal evolution of SST and low-level wind anomalies in the Indian Ocean prior to and concurrent with the Indian summer monsoon and the impact on the regional moist static energy (MSE) budgets using observational and reanalysis data (Sections 4.3 and 4.4). From this analysis, and results of idealized AGCM simulations (Section 4.5), we propose a hypothesis for the delayed effect of El Niño on the Indian monsoon rainfall.

[1] The definition of "early" versus "late" monsoon seasons is somewhat arbitrary. However, since the anomalous surface latent heat flux begins rebounding in August [see Section 4-3b] and has maximum effect in September, we contrast the AS period with the JJ period.

4.2. Data sets and Model

4.2.1. Data sets

We investigate the seasonal evolution of the SST and MSE budget using the European Centre for Medium Range Weather Forecasts 40 year Reanalysis (ECMWF ERA-40; Uppala et al. 2005). The ERA-40 SSTs are based on monthly Met Office Hadley Centre SST data (HadISST; Rayner et al. 2003) up to October 1981, and the weekly Reynolds optimum interpolation version-2 data (Reynolds et al., 2002) thereafter. Because the long-term SSTs are based on observations, the low-level specific humidity field, which is strongly dependent on the SSTs, will be able to provide reliable and consistent MSE budgets. We use the version of ERA-40 produced by NCAR's Data Support Section (**http://www.cgd.ucar.edu/cas/catalog/ecmwf/era40)** consisting of monthly means for 256x128 regular Gaussian grids at T-85 spectral truncation and 23 pressure levels spanning September 1957 to August 2002.

We used a 23-year (1979-2001) monthly long-term mean to calculate the climatological mean of individual variables, such as surface latent heat flux, SST, individual vertical level winds and specific humidity. The SST, surface latent heat flux, and specific humidity of the individual vertical levels were linearly detrended due to their increasing trend from the 1960s to the 1990s. However, the individual MSE budgets during major El Niño events that we will present are qualitatively consistent (or, almost identical) regardless of the long-term linear detrending, except that the magnitudes of anomalous SST and the anomalous MSE budget get weaker by 20% for the 1982-83 event in case the linear detrending is not applied.

For monsoon precipitation, the Climate Prediction Center (CPC) Merged Analysis of Precipitation (CMAP; Xie and Arkin 1997) data set was used. The CMAP data consist of monthly means at a horizontal resolution of 2.5° x 2.5° spanning January 1979 to December 2005. For the CMAP data, climatological means were estimated for the entire period (1979-2005) of coverage, and anomalies were formed as for the ERA-40 fields. The precipitation anomalies of two major El Niño events are quite robust regardless of the specific averaging periods for the climatological mean calculation.

4.2.2. Model

To understand the role of remote forcing from the eastern equatorial Pacific and its temporal evolution, we conducted a set of simplified AGCM experiments. We used the Community Climate Model 3.10 (CCM3; Kiehl et al. 1998) at T31x15 horizontal resolution (i.e., triangular truncation of 31 basis functions in the meridional and 15 in the zonal) and the standard 18 levels in the vertical. A revised convective parameterization closure (Zhang and Mu 2005, hereafter ZM05) based on the Zhang-McFarlane scheme was implemented. Under the ZM05 scheme, convective closure consists of large-scale forcing of temperature and humidity in the free troposphere rather than convective available potential energy as in the original scheme. We find that the revised convection scheme is superior to the standard CCM3 convection scheme (Zhang and McFarlane 1995) in simulating the Indo-Pacific tropical climate: in particular, the ZM05 scheme increases western Pacific monsoon precipitation, thereby alleviating the negative

precipitation bias seen in the original convection scheme by Zhang and McFarlane (1995); it also removes the spurious heavy precipitation over the Arabian Peninsula simulated by the original convection scheme.

The CCM3 was coupled to a 30m constant mixed layer slab ocean model at all ocean grid points outside of the tropical Pacific (20°S - 20°N, 160°E - 270°E) where SST was prescribed with values corresponding to total SSTs from February of the growing year (either 1982 or 1997) to November of the decaying year (1983 or 1998). The SST forcing was derived from the gridded, 2° x 2° monthly-mean NCEP-Reynolds historical global SST field covering January 1950 - December 2000 (Reynolds and Smith 1994). For the slab ocean grid points, a climatological monthly Q-flux correction was applied to ensure that the simulated SST seasonal climatology closely matches the observed SSTs (Reynolds and Smith 1994). Twelve ensemble members were simulated for each El Niño event, with each ensemble member initialized from a distinct set of self-consistent atmospheric conditions on February 1 of the growing year. The initial conditions were extracted from a long-term simulation integrated with the climatological seasonal cycle SSTs imposed in the central and eastern tropical Pacific (20°S - 20°N, 160°E - 270°E) and a Q-flux adjusted uniform 30m slab ocean elsewhere.

4.3. North Indian Ocean warming and the monsoonal low-level winds

4.3.1. North Indian Ocean warming

A Hovmoller plot of anomalous SSTs (Figures 4-2a and 4-2b) demonstrates that a warming of the NIO occurs in the summer monsoon season after major El Niño events. Here, the longitudinal averaging interval (40°E - 90°E) covers the entire Western Indian Ocean including the Arabian Sea and part of the Bay of Bengal; this interval was selected since the SSTs and winds over the Arabian Sea and the western part of the Bay of Bengal effectively modulate the Indian monsoon convective strength through the low-level westerly monsoon flow. Also, the monsoonal winds and SST vary more over the Arabian Sea region than the eastern part of the Bay of Bengal or the South China Sea during the major El Niño events.

The 1983 event exhibited strong NIO warming, i.e., the SSTs increased rapidly from climatological conditions, during late boreal spring (May-Jun) and persisted until Jul-Aug. The 1983 event suggests northward progression of positive SST anomalies from the South Equatorial Indian Ocean during the boreal spring into the NIO region by the summer monsoon season (Figure 4-2a). The 1998 event had a warm NIO in the summer monsoon season as well (Figure 4-2b), although the signal is weaker compared to the 1983 event. Also, the anomalously warm NIO existed in the spring, leading to a double warming signal (in the spring and the summer) over the NIO (Figure 4-2b). This double warming signal is reminiscent of structure in the regression of the winter (Nov-Dec-Jan) Niño3.4 index on the subsequent spring to summer Indian Ocean SSTs in Du et al. (2009).

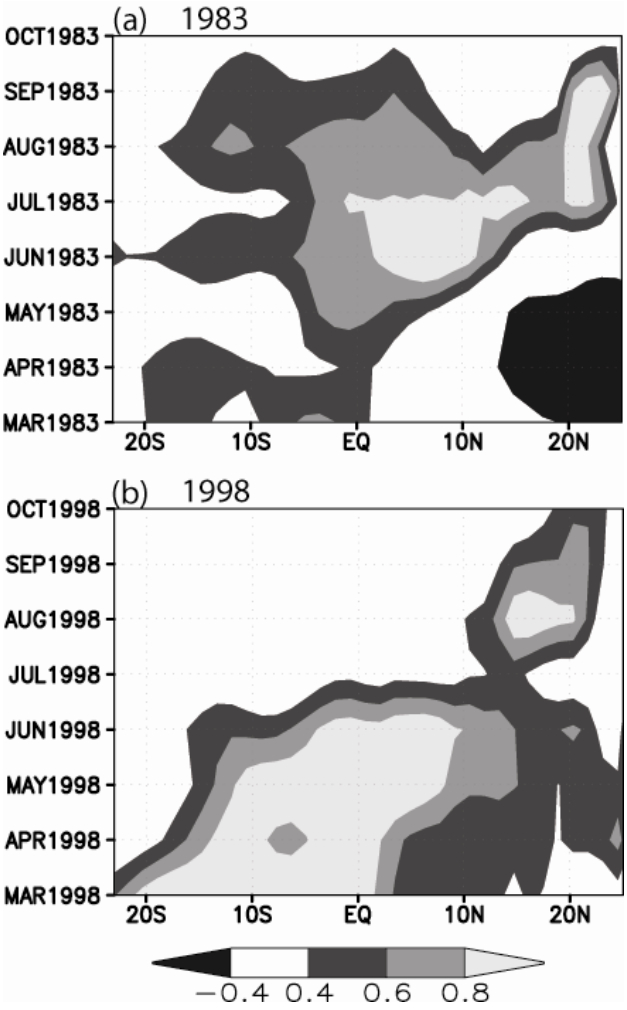

FIG. 4-2: Hovmoller diagram (40°E - 90°E longitudinal mean) of anomalous ERA-40 SST (K) following the (a) 1982-83 and (b) 1997-98 major winter El Niño events.

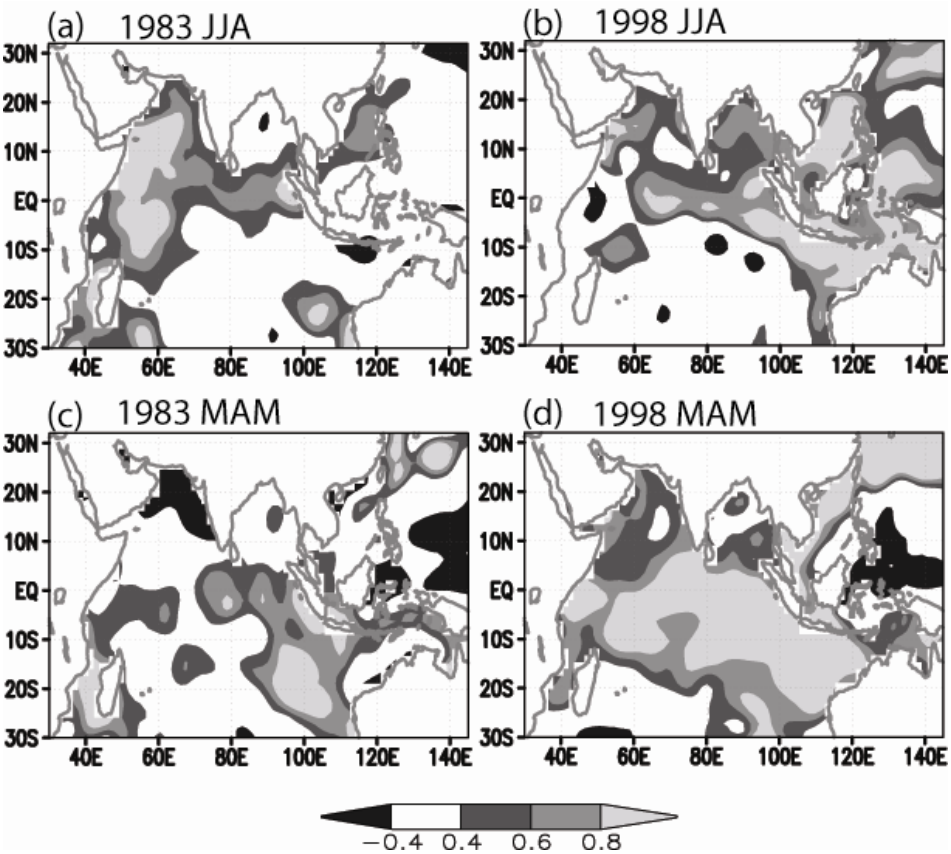

FIG. 4-3: Seasonal transitions of anomalous ERA-40 SSTs (K) during the summer monsoon season (Jun-Jul-Aug) for the (a) 1983 and the (b) 1998. (c) and (d) are same as (a) and (b) but for the spring season (Mar-Apr-May).

The detailed longitude-latitude structure of the SST anomalies for the two events contains some substantial differences. The 1983 event has positive SST anomalies over the Southeast Indian Ocean in spring (Figure 4-3c), and a strong warming signal appears over the Arabian Sea in the summer (Figure 4-3a). On the other hand, the 1998 event has very strong warm SST anomalies in the Equatorial and South Equatorial Indian Ocean in spring (Figure 4-3d), which may have been supported by stronger equatorial Ocean wave activities (Webster et al. 1999) or large-scale tropical troposphere warming (Chiang and Lintner 2005). The South Equatorial warm SST anomalies during the spring of 1998 dissipate by the summer monsoon season, whereas the warm NIO signal slightly strengthens (Figure 4-3b). The maximum warm SST anomalies exist over the Western Pacific in the summer of 1998, whereas the 1983 event has its maximum warm anomalies over the Arabian Sea.

Although there are clearly differences between the 1983 and 1998 events, we emphasize here two common features, namely (i) the distinctly warm NIO throughout the summer monsoon season, and (ii) dissipation of the South Equatorial Indian Ocean warming signal by monsoon onset.

4.3.2. Monsoonal low-level winds and surface latent heat flux

Hovmoller plots of anomalous surface wind speeds (50°E - 83°E mean: mostly over the Arabian Sea region, where strong monsoonal low-level winds blow) indicate weakening of NIO-region surface wind speeds during the early phase of the monsoon followed by a later rebound toward climatological values for both El Niño events (contour lines of Figure 4-4a and 4-4b). Since the area-averaged (50°E - 83°E mean) monthly standard deviations of surface wind speed during the summer monsoon season (JJAS mean from the monthly mean ERA-40) is only ~0.3 m/s, the observed early season weakening (0.5 m/s) is rather substantial. Although both events consistently show the weakening of the low-level winds and the surface latent heat suppression from the late spring to the mid-monsoon season, the timing of wind speed recovery toward climatology slightly differs in each case. For the 1983 case, the weakening starts in May and peaks in June, maintaining the weakening signal by July. The wind speed begins to rebound in August and grows substantially stronger than the seasonal mean in September. On the other hand, for the 1998 event, the weakening persists longer, peaking in August, with some recovery evident in September.

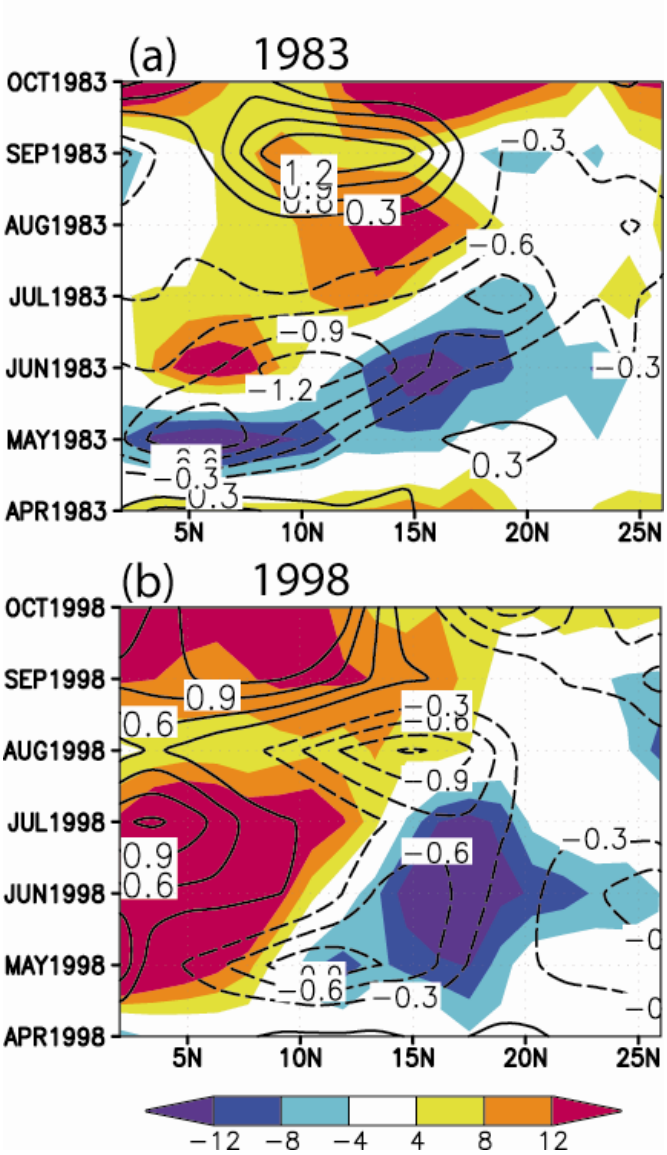

FIG. 4-4: (a) Hovmoller diagram (50°E - 83°E longitudinal mean) of anomalous ERA-40 surface latent heat flux (shadings: warm colors imply more evaporation from the surface than the seasonal mean, in W m^{-2}) and anomalous surface wind speed (contours: m s^{-1}) for the (a) 1982-83 and the (b) 1997-98 events.

Figures 4-4a and 4-4b also show that a suppression of the latent heat flux (LHF) is coincident with the weakening of winds both for the 1983 and 1998 events, although the latter slightly lags the LHF. Here, we hypothesize that the surface wind weakening might be the principal driver of the NIO warming. To verify this, we decomposed the surface evaporation perturbations into dynamic and thermodynamic contributions, following Chikamoto and Tanimoto (2006). The surface latent heat flux anomaly is linearized as:

$$LHF' \approx \kappa\left[W'(\overline{q}_* - \overline{q}_a) + \overline{W}(q'_* - q'_a)\right] \quad (4.1)$$

where q_* is the saturation specific humidity at the sea surface; q_a is the specific humidity at a reference level near the sea surface; W is the surface wind speed, and κ is a bulk coefficient. The first term on the RHS (the dynamic contribution) is associated with wind speed changes, while the second term (the thermodynamic contribution) is associated with the humidity difference changes. Assuming constant κ, the dynamic contribution dominates the NIO LHF suppression during the monsoon onset period (not shown), though since the assumption of constant κ can be unrealistic and the ocean dynamics are neglected, we are not confident in providing the exact magnitude of wind effect. Rather, we suggest that the contribution from the weakening of monsoonal winds is a nontrivial factor for the NIO warming.

The persistent NIO warming leads to an increased LHF during the decaying period of the monsoon. The LHF signal leads the surface wind signal because the warmer NIO increases the LHF to the atmosphere, compensating the effect from the weaker surface wind speed. Additionally, the rebound of surface wind strength during the late monsoon season may also contribute to increasing the LHF. One caveat worth noting is that the LHF rebound is limited to the Arabian Sea, whereas the Bay of Bengal consistently experiences LHF suppression because of persistent weakening of surface winds throughout the summer monsoon season (not shown).

4.4. Moisture transport and moisture stability over the NIO

While the occurrence of positive rainfall anomalies during the late monsoon season (Figure 4-1b) is consistent with anomalous LHF, how do we explain the above normal rainfall in the early season? In a dynamical sense, the substantially weaker surface winds and the reduced LHF during the early seasons of both events suggest a weakened monsoon, although the rainfall is slightly above normal or close to normal (Figures 4-5a and 4-5b)[2]. The paradox of the increased monsoon rainfall associated with the weaker monsoon circulation has been previously addressed by a few GCM studies under global warming scenarios (Kitoh et al. 1997; Stowasser et al. 2009).

As we presented, the paradox seems to appear at the inter-annual timescale as well. To explain the mechanism, we examine the anomalous moist processes associated with the warmer NIO, specifically changes to horizontal moisture transport and moist stability over the NIO.

[2] We present Jun-Jul-Aug mean precipitation to smooth out monsoon intraseasonal variability. Use of the Jul-Aug-Sep or Aug-Sep mean precipitation indicates stronger monsoon rainfall over the Indian subcontinent for both the 1983 and 1998 events (not shown).

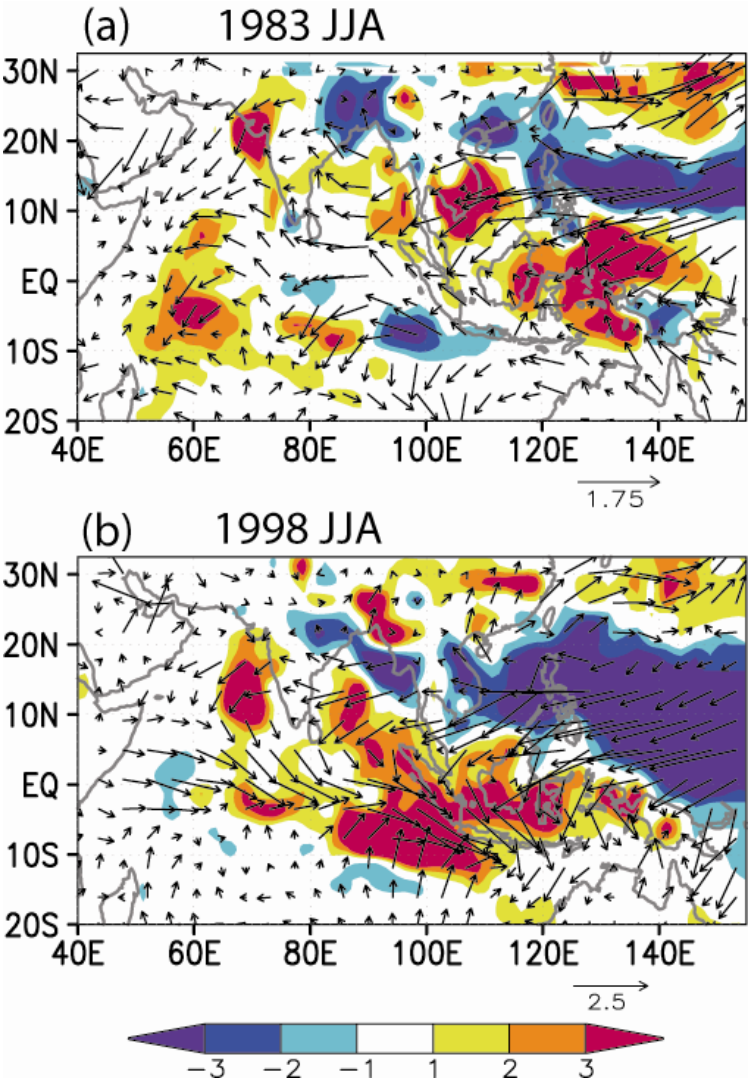

FIG. 4-5: Jun-Jul-Aug mean CMAP precipitation anomalies (shadings: mm day^{-1}) and ERA-40 surface wind anomalies (vectors: m s^{-1}) for the (a) 1983 and the (b) 1998.

4.4.1. Moist Static Energy (MSE) budget methodology

Following Chou and Neelin (2004) and Chou et al. (2006), the anomalous vertically integrated MSE, <h>', can be written as:

$$\frac{\partial}{\partial t} < h >' + < \vec{\omega} \frac{\partial h}{\partial p} >' = - < \vec{v} \cdot \nabla_H h >' + F_{net}' \qquad (4.2)$$

where $'$ denotes a perturbation; $< >$ represents vertical integration from the surface layer (1000 hPa) to near the tropopause height (150 hPa); and v and ω are the horizontal wind and pressure velocity individually. F_{net} denotes net energy input into the atmosphere column, including both net radiative flux and surface heat flux. Because of rapid atmospheric adjustment, $\frac{\partial}{\partial t} < h >'$ can be neglected on

monthly timescales. Given our interest in convective energy variations associated with anomalous vertical motions, the second term on the LHS of (4.2), i.e., vertical advection of MSE, can be linearized by separating perturbations and climatological means. Equation (4.2) is then rearranged to:

$$< \omega' \frac{\partial \bar{h}}{\partial p} > \approx < -\overline{\omega} \frac{\partial q'}{\partial p} > + < -\overline{\omega} \frac{\partial s'}{\partial p} > + < -v \cdot \nabla_H q >' + < -v \cdot \nabla_H s >' + F_{net}' \qquad (4.3)$$

where the perturbation moisture and dry static energy ($s = C_p T + gZ$) terms have been explicitly separated. In this framework, the LHS of (4.3), which is proportional to the anomalous vertical motion, provides a measure of the anomalous large-scale convective activity; the terms on the RHS represent a diagnostic budget for these motions. The first term on the RHS of (4.3), $< -\overline{\omega} \frac{\partial q'}{\partial p} >$, is analogous to the anomalous moist stability, Mq' (Chou et al. 2006). Over the equatorial ocean region, the moisture transport $< -v \cdot \nabla q >'$ is usually much larger than the dry static energy advection $< -v \cdot \nabla s >'$, although the magnitude of the dry static energy advection, especially temperature advection, becomes nontrivial where tropospheric temperature gradients become large (e.g., near land-ocean interfaces). The anomalous dry static stability, $< -\overline{\omega} \frac{\partial s'}{\partial p} >$ tends to compensate the Mq'; however, the magnitude of compensation is limited, around one third of Mq' over the NIO (not shown).

4.4.2. Moist stability and moisture transport over the NIO

The JJA mean Mq' is mostly positive over the vast warm pool region, covering the NIO and the western Pacific for both events (Figures 4-6a and 4-6b). $Mq' > 0$ occurs with strengthened moist convection over the ocean regions adjacent to the Indian subcontinent, although its relationship to continental convection looks less obvious. Even though the Arabian Sea has higher SST anomalies than the Bay of Bengal region (see the 1983 event, Figure 4-3a), Mq' is more strongly positive over the Bay of Bengal than the Arabian Sea since upward motions are stronger and the moisture stratification effect is more efficient over the former.

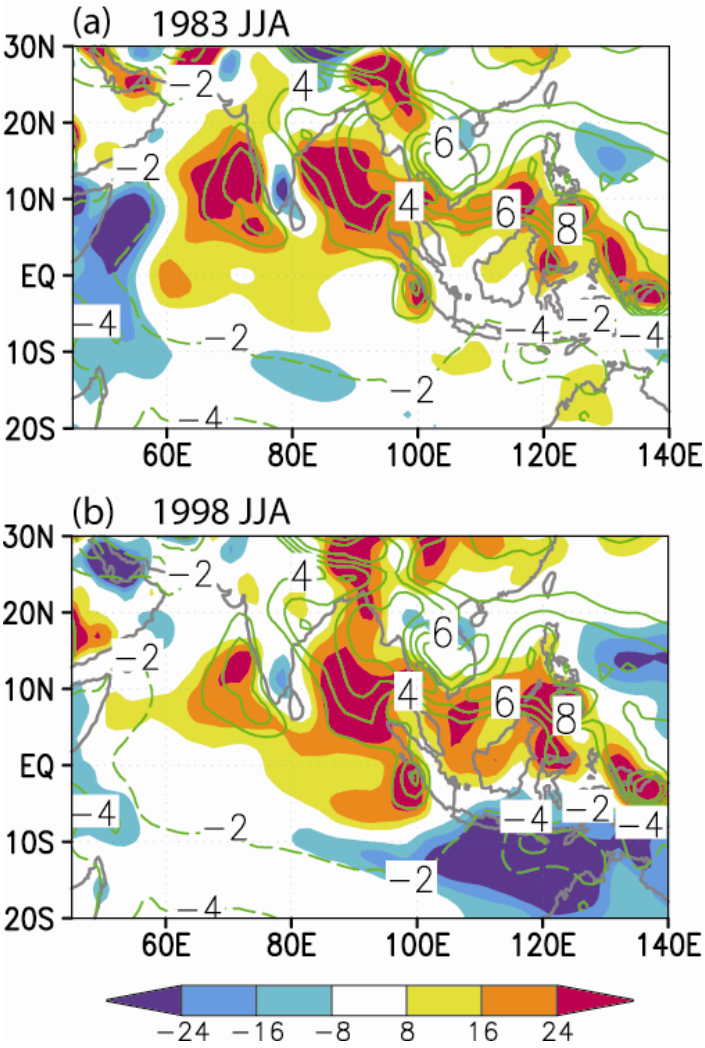

FIG. 4-6: Jun-Jul-Aug mean anomalous moist stability (warm colors contribute to strengthening the moist convection in W m^{-2}) for the (a) 1983 and the (b) 1998 events. Green contours indicate the pressure velocity (positive values imply upward motion). The units are 0.01 pa s^{-1}.

We suggest that the warmer NIO-induced Mq' has some similarities to the rich-gets-richer mechanism under global warming (Chou et al., 2006 and 2009). As shown in Chou et al. (2009), application of the MSE budget to 10 coupled global climate models under a global warming scenario indicates that $Mq' > 0$ occurs in all models when the mean vertical motion field is upward. That is, over oceanic convecting regions, where the mean large-scale vertical motion is upward, the large-scale lower-troposphere moistening under global warming tends to enhance tropical precipitation. Similarly, the spatial patterns of Mq' between the 1983 and 1998 events are consistent with each other, showing strong consistency with the seasonal mean vertical motion field (contour lines of Figures 4-6a and 4-6b), regardless of the detailed SST patterns.

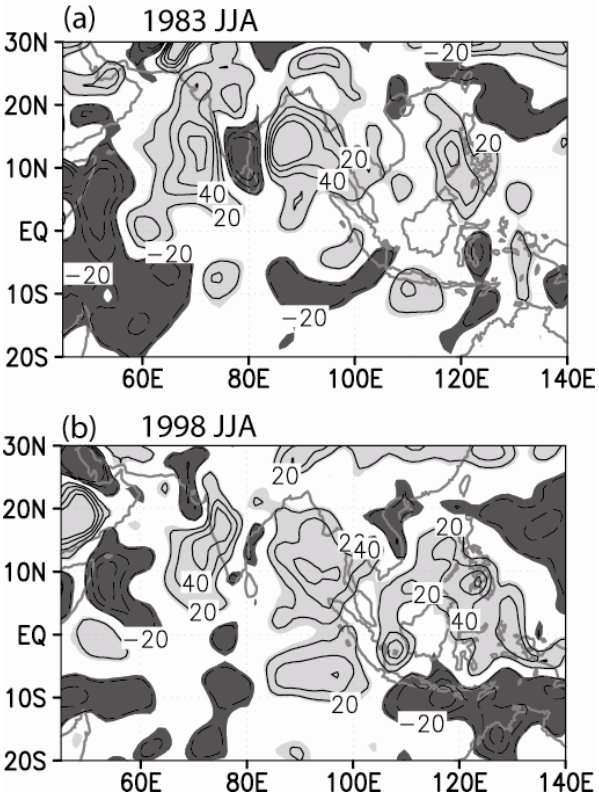

FIG. 4-7: Total moist process: anomalous moisture transport plus anomalous moist stability (in W m^{-2}) for the (a) 1983 and the (b) 1998. Light (dark) shadings contribute to strengthening (weakening) of the moist convection. Absolute values higher than 20 are shaded and the contour interval is 20 W m^{-2}.

The Indian Ocean warming and the subsequent moisture effect to the continental region become more obvious when the moisture transport is considered. Figures 4-7a and 4-7b indicate that the combined effect of Mq' and the moisture transport, $<-v\cdot\nabla q>'$, contributes to increasing the basin-wide monsoon rainfall. The JAS and AS mean total moist processes also indicate positive monsoon convective strength with similar magnitude with the JJA mean (not shown). The box-averaged (60-100E and 10-25N) JJAS mean combined moist energy is about 30 (34) W/m^2 for the 1983 (1998) event. These values appear significant given that the JJAS mean standard deviation of the combined moist energy during the period of 1979 to 2001 is about 18 W/m^2. However, these values should be interpreted as rough approximations, especially given the lack of information about finer spatial and temporal scales. For example, using daily ERA-40 and NCEP reanalysis data sets, Back and Bretherton (2006) demonstrated substantial magnitude of non-conserving small source terms (or residuals) in the MSE budget. Therefore, the MSE budget estimated from monthly-mean data likely has a larger bias. Here, we only suggest that the warmer NIO-induced reduced moist stability and stronger moisture transport may be major mechanisms for compensating the weaker monsoon circulation effect during the early to mid-monsoon season as well as for increasing the rainfall during the late monsoon season.

4. 5. The effects of El Nino's residual signal on the North Indian Ocean warming

In the absence of NIO warming, the warmer Equatorial Indian Ocean alone would reduce the monsoon rainfall over the Indian subcontinent. For example, Chung and Ramanathan (2006) prescribed a warmer Equatorial Indian Ocean in their AGCM and found that an anomalous northward decreasing SST profile weakens Indian monsoon rainfall, while uniform Indian Ocean warming strengthens it. Given that the warm off-equatorial SIO signal largely dissipates by the early monsoon season, how are the warm NIO SSTs maintained and even strengthened (up to 1.5K) during the summer monsoon season?

As discussed in Section 4.3, the ERA-40 SSTs (Figures 4-2a and 4-2b) indicate peak NIO warming signal in Jul-Aug, or two seasons after the El Niño peak. This lag is intriguing because the NINO3 (or NINO 3.4) SST anomalies are significantly attenuated by this time. Is the contemporaneous influence of (weak) Eastern Equatorial Pacific conditions persisting through spring or early summer monsoon season following El Niño sufficient to drive the peak NIO warming? Or, does some other mechanism, e.g., the effect of local Indian ocean-atmosphere feedback processes, provide a bridge to the peak winter forcing? In order to address this, we introduce an idealized experimental set-up.

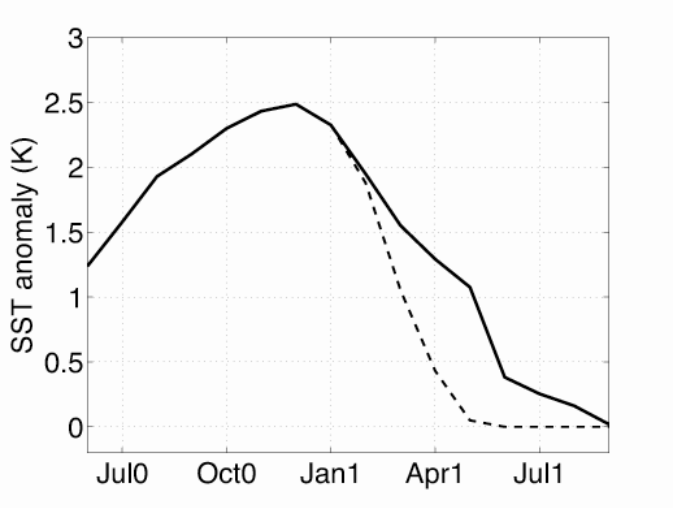

FIG. 4-8: SST anomalies (20S~20N and 210E~260E mean) imposed in idealized El Niño experiments using CCM3. The solid curve is the original "Spring El Niño" experiment and the dotted curve is "No-Spring El Niño" sensitivity experiment (see Section 5a).

4.5.1. Experimental design

Although the 1982-83 and 1997-98 forcing experiments have their peak forcing during boreal winter, some warming of the Eastern Equatorial Pacific persists through the end of the monsoon season (Figure 4-8; solid line). In the idealized experiment discussed here, we simply eliminated the anomalous SST forcing immediately preceding (and during) the monsoon season by relaxing the SST anomalies to zero over February 1983 (or 1998) to May, as in Figure 4-8 (dotted line). This experiment (hereafter referred to as the "No-Spring El Niño" case) effectively removes the

influence of El Niño's "tail" on the monsoon. By comparing the "No-Spring El Niño" case to the case considered previously (referred to hereafter as the "Spring El Niño" case; solid line in Figure 4-8), it is possible to isolate the effect of contemporaneous El Niño forcing from the delayed effect of winter El Niño conditions. Since the simulations for both events produced similar results, we focus here on the 1997-98 results only.

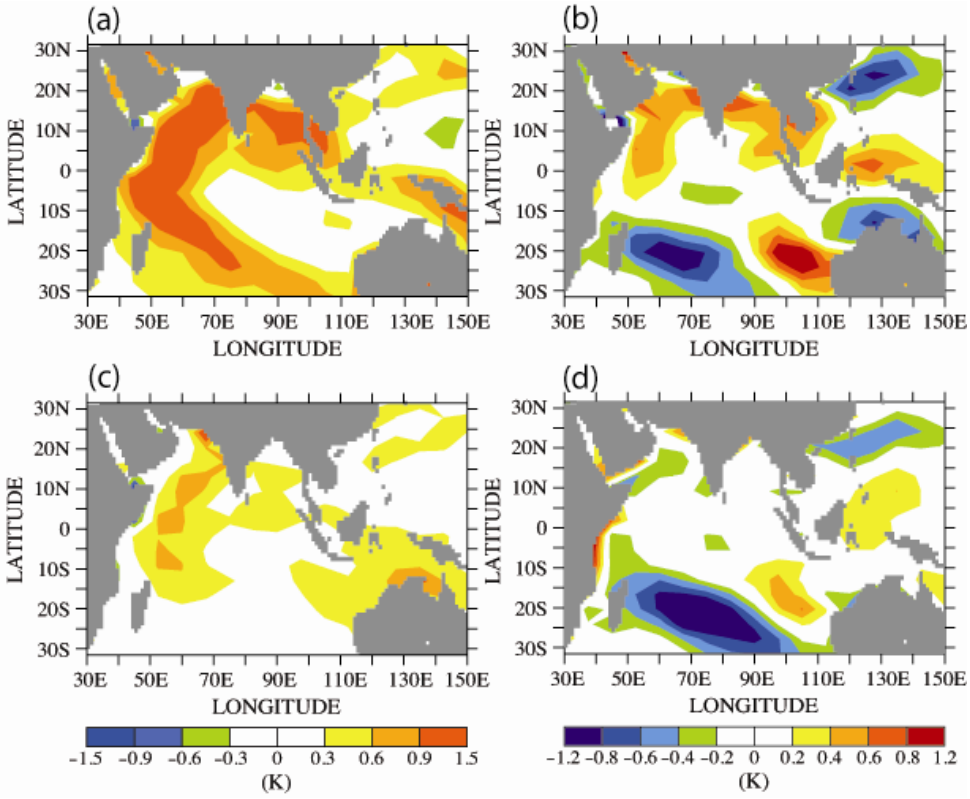

FIG. 4-9: Anomalous SSTs simulated by the Spring El Niño experiment. (a) Jul-Aug mean (K) and (b) the difference between the Jul-Aug mean and the May-Jun mean (Jul-Aug minus May-Jun). (c) and (d) are same as (a) and (b) but for the No-Spring El Niño experiment.

4.5.2. Role of El Nino's tail on the NIO warming

The CCM3 perturbation experiment simulates the NIO warming in Jul-Aug, with values up to 1.5C warmer than the climatological Jul-Aug mean (Figure 4-9a). The difference between the Jul-Aug SST and the late-spring (May-Jun) SST anomalies illustrates the meridional evolution of the anomalous SST field, with the NIO (SIO) warming (cooling) in Jul-Aug relative to May-Jun (Figure 4-9b). The suppression of NIO LHF during the onset period of the monsoon (Figure 4-10a) and its rebound it during the late season (Figure 4-10b) are also captured.

Although our idealized El Nino experiment does simulate the Arabian Sea warming in the early monsoon season, which is similar to the ERA-40 1983 SST anomalies, the detailed spatial patterns of the NIO warming are quite different from the ERA-40 SSTs. For example, the

observed Western Pacific warming during the 1998 is not captured. Also, the simulated latent heat flux rebound occurs in both the Arabian Sea and the Bay of Bengal (Figure 4-10b), whereas ERA-40 indicates consistent suppression of the LHF over the Bay of Bengal (not shown). Despite these detailed differences between the model and the reanalysis, we argue that our idealized El Niño model setup captures the salient mechanistic features, such as the weakening of monsoonal winds, pre-monsoon suppression of LHF, and the subsequent NIO warming during monsoon onset.

Examination of the No-Spring El Niño case does show NIO warming at the onset of the monsoon suggesting a role for the peak El Niño forcing, although the amplitude is less than half when spring El Niño conditions are included (Figures 4-9c and 4-9d). Figures 4-10c and 4-10d illustrate differences of the low-level winds and the LHF over the NIO between the Spring El Niño and No-Spring El Niño experiments. The magnitudes of low-level wind speed anomalies and the LHF anomalies between Figures 4-10a and Figure 4-10c are quite close, suggesting that early monsoon season weakening of low-level winds and LHF suppression are mostly from spring El Niño conditions. Because the Spring El Niño strongly suppresses the LHF in the early period and thereby warms the NIO, there is a larger rebound of the LHF during the late period (Figures 4-10b and 4-10d).

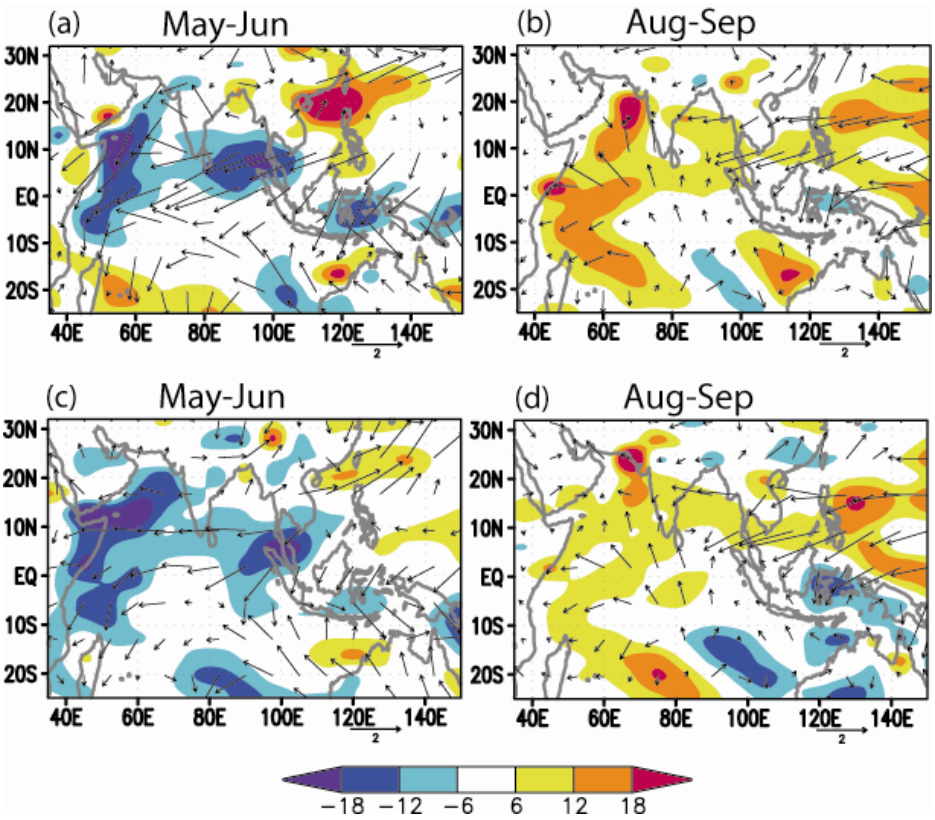

FIG. 4-10: Anomalous surface latent heat flux (warm colors imply more evaporation from the surface than seasonal mean, in W m^{-2}) simulated by the Spring El Niño experiment during (a) May-Jun and (b) Aug-Sep. Vectors indicate surface wind anomalies (m s^{-1}). Also shown are

differences in the surface latent heat flux and surface wind anomalies between the Spring El Niño experiment and No -Spring El Niño experiments during (c) May-Jun and (d) Aug-Sep.

These results confirm that the residual El Niño region SSTs in the Eastern Equatorial Pacific, although attenuated relative to peak winter conditions, play a crucial role for the NIO warming in the CCM3 simulations. However, the configuration of these experiments has some limitation in elucidating the effect of internal feedback process between the Indian Ocean and the Northwestern subtropical Pacific. For example, Watanabe and Jin (2003) found in their simplified moist baroclinic model that anomalous surface highs over the Philippine Sea are maintained by the local tropical Indian Ocean warming as well as El Niño's direct subsidence effects over the Philippine Sea. Based on various GCM experiments, Annamalai et al. (2005) infers that the El Niño-induced warm tropical Indian Ocean SSTs explains more than 50% of the anomalous surface anticyclones over the Philippine and South-China Sea. A recent GCM study by Xie et al. (2009) suggests advanced dynamics on the interactions between the warmer NIO and the Philippine anticyclones, i.e., a warmer NIO generates eastward propagating atmospheric Kelvin waves, which would maintain surface highs in the Northwestern subtropical Pacific.

In our case, it is not clear if the remnant warm El Niño condition in the Eastern Equatorial Pacific directly reduces the monsoonal low-level winds, or if the warm tropical Indian Ocean induced by the persistent Spring El Niño weakens the low-level winds and generates the anomalous Philippine anticyclone. Regardless of the causality, we suggest that the Spring El Niño signal, persisting into the onset period, is a potential source for weakening the monsoonal winds and maintaining the anomalously warm NIO throughout the summer monsoon season.

4.6. Summary and discussion

We have demonstrated that the influence of a major winter El Niño event persists into the Indian summer monsoon season via an anomalously warm NIO, with the latter in turn driving an increase of rainfall over the NIO and neighboring Indian subcontinent. The weakening of low-level monsoonal winds and the suppression of surface latent heat flux during the late spring and the onset period of the monsoon consistently occur both for the 1983 and 1998 El Niño events. The weakening of winds persists into the mid-monsoon season, but the monsoon rainfall remains close to its climatological mean. Anomalous moist processes tied to the warmer NIO, such as the reduced moist stability and the increased horizontal moisture advection, seem able to compensate the weakened monsoon circulation effect. Idealized CCM3 experiments demonstrate that the strong NIO warming present at the onset of the monsoon season arises in response to residual warm SSTs in the Eastern Equatorial Pacific, which persist into the late spring and early summer seasons. This remote warming appears to be linked to low-level monsoonal wind weakening and substantial suppression of the surface LHF (~30% lower than the seasonal mean), thereby warming the NIO during the onset period of monsoon. However, the detailed pathway connecting monsoonal wind weakening to residual eastern Pacific SSTs is unclear. Specifically, we are unable to quantify the relative importance of the remote atmospheric subsidence effect associated with the remnant warm El Niño condition (an anomalous forced Walker circulation) and internal circulation feedback processes initiated by the warm NIO. A possible example of the latter, the anomalous Philippine anticyclone,

contribute to weakening the low-level winds, which in turn warms the NIO. The NIO-induced internal feedback may also be related to the precise timing of the monsoonal low-level wind rebound during the late monsoon season. Specifically, we still do not know why weaker monsoonal winds persisted into August during the 1998 event, whereas they rebounded a month earlier during the 1983 event. Further investigation on the feedback processes between the NIO and the Philippine surface anticyclones may elucidate the mechanisms as well as the timing of the monsoonal low-level winds rebound during the late monsoon season.

The most significant insight we can provide at this stage is that El Niño's decay, if it occurs sufficiently slowly to maintain Eastern Pacific SSTs into the spring season, is a useful index for predicting the Indian monsoon rainfall and the monsoon circulation strength. Another interesting result is that the monsoonal low-level wind strength does not necessarily represent the monsoonal convective strength. Rather, moist processes, such as moist stability and moisture transport associated with the warmer NIO, can compensate for the wind effect. In particular, the weakening of winds can warm the NIO, with the latter increasing the monsoon region rainfall by reducing the moist stability and increasing the horizontal moisture advection. This compensation points to the complexity of the Indian monsoon climate system, for which the interannual variability may not be readily categorized by a simplified circulation index or SSTs. In terms of prediction, we argue for the importance of considering the slowing-varying time evolution of the SSTs adjacent the Indian subcontinent (Shukla 2007), specifically if it is in the warming phase or in the cooling (i.e., warm SSTs relax back to normal condition) phase. As we indicated, the delayed effect is most obvious during the cooling phase when both the moist process and low-level winds act in concert to strengthen monsoon convection.

5. References

Annamalai, H., P. Liu, and S.-P. Xie, 2005: Southwest Indian Ocean SST variability: Its local effect and remote influence on Asian monsoons. *J. Climate.*, **18,** 4150-4167.

Back, L. E. and C. S. Bretherton, 2006: Geographic variability in the export of moist static energy and vertical motion profiles in the tropical Pacific. *Geophys.Res. Lett.*, **33,** L17810.

Boos, W. R., 2008: Wind-evaporation feedback, angular momentum conservation, and abrupt onset of monsoons. *Ph.D dissertation at MIT*.

Boos, W. R. and Z. Kuang, 2009: Dominant control of the South Asian monsoon by orographic insulation versus plateau heating. *Nature*, **463**, 218-222.

Bordoni, S. and T. Schneider, 2008: Monsoons as eddy-mediated regime transitions of the tropical overturning circulation. *Nature Geoscience*, **1**, doi:10.1038/ngeo248.

Bracco, A., F. Kucharski., F. Molteni., W. Hazeleger and C. Severijns, 2007: A recipe for simulating the interannual variability of the Asian summer monsoon and its relation with ENSO. *Clim Dyn.*, doi: 10.1007/s000382-006-0190-0.

Chang, E. K. N., 1993: Downstream development of baroclinic waves as inferred from regression analysis. *J. Atmos. Sci.*, **50**, 2038-2053.

Chang, E. K. N., and I. Orlanski, 1993: On the dynamics of a storm track. *J. Atmos. Sci.*, **50**, 999-1015.

Chang, E. K. N., and D. B. Yu, 1999: Characteristics of wave packets in the upper troposphere. Part I: Northern Hemisphere winter. *J. Atmos. Sci.*, **56**, 1708-1728.

Chang, E. K. N., 2001: GCM and observational diagnoses of the seasonal and interannual variations of the Pacific storm track during the cool season. *J. Atmos. Sci.*, **58**, 1784-1800.

Charney, J. G. and A. Eliassen, 1949: A numerical method for predicting the perturbations of the mid-latitude westerlies. *Tellus*, **1**. 38-54.

Chiang, J. C. H. and A. H. Sobel, 2002: Tropical tropospheric temperature variations caused by ENSO and their influence on the remote tropical climate. *J. Climate.*, **15**, 2616-2631.

Chiang, J. C. H. and B. R. Lintner, 2005: Mechanism of remote tropical surface warming during El Nino. *J. Climate.*, **18**, 4130-4149.

Chikamoto Y., and Y. Tanimoto, 2006: Air-sea humidity effects on the generation of tropical Atlantic SST anomalies during the ENSO events. *Geophys. Res. Lett.*, **33**, L19702.

Cook, K. H. and I. M. Held, 1992: The Stationary response to large-scale orography in a General Circulation Model and a Linear Model. *J. Atmos. Sci*, **49**, 525-539.

Chou, C. and J. D. Neelin, 2003: Mechanisms limiting the northward extent of the northern summer monsoons over North America, Asia and Africa. *J. Climate*, **16**, 406-425.

Chou, C. and J. D. Neelin, 2004: Mechanisms of global warming impacts on regional tropical precipitation. *J. Climate.*, **17**, 2688-2701.

Chou, C., J. D. Neelin, J.-Y. Tu, and C.-T. Chen, 2006: Regional tropical precipitation change mechanisms in ECHAM4/OPYC3 under global warming. *J. Climate*., **19**, 4207-4223.

Chou, C., J. D. Neelin, C.-A. Chen, and J.-Y. Tu, 2009: Evaluating the "rich-get-richer" mechanism in tropical precipitation change under global warming. *J. Climate*, **22**, 1982-2005.

Chul, E. C. and V. Ramanathan, 2006: Weakening of north Indian SST gradients and the monsoon rainfall in India and the Sahel. *J. Climate.*, **19**, 2036-2045.

Deng, Y., and M. Mak, 2005: An idealized model study relevant to the dynamics of the midwinter minimum of the Pacific storm track. *J. Atmos. Sci.*, **62**, 1209-1225.

Du, Y., S.-P. Xie, G. Huang, and K. Hu, 2009: Role of air-sea interaction in the long persistence of El Nino-induced North Indian Ocean warming. *J. Climate*, **22**, 2023-2038.

Eady, E. T., 1949: Long waves and cyclone waves. *Tellus*, **1**, 33-52.

Emanuel, K. A., J. D. Neelin, and C. S. Bretherton, 1994: On large-scale circulations in convecting atmosphere. *Quart. J. Roy. Meteorol. Soc*, **135**, 319-335.

Farrell, B., 1984: Modal and non-modal baroclinic waves. *J. Atmos. Sci*, **41**, 668-673.

Gill, A. E., 1980: Some simple solutions for heat-induced tropical circulation. *Quart. J. Roy. Meteorol. Soc*, **106**, 447-462.

Gill, A. E., 1982: *Atmosphere-Ocean Dynamics*. Academic Press.

Hahn, D. G. and S. Manabe, 1975: The role of mountains in the South Asian monsoon circulation. *J. Atmos. Sci*, **32**, 1515-1541.

Hakim, G. J, 2003: Developing Wave Packets in the North Pacific storm track. *Mon. Weather. Rev.*, **131**, 2824-2837.

Harnik, N., and E. K. M. Chang, 2004: The effects of variations in jet width on the growth of baroclinic waves: Implications for midwinter Pacific storm-track variability. *J. Atmos. Sci.*, **61**, 23-40.

Held, I. M, and B. J. Hoskins, 1985: Large-scale eddies and the general circulation of the troposphere. *Advances in Geophysics*., **28**.

Held, I. M., M.-F. Ting, and H.-I. Wang, 2002: Northern Winter Stationary Waves: Theory and Modeling. *J. Climate*, **15**, 2125-2144.

Held, I. M., M. Ting, and H. Wang, 2002: Northern winter stationary waves: Theory and modeling. *J. Climate*, **15**, 2125-2144.

Huang, B. and J. Shukla., 2005: On the Mechanisms of the Interannual Variability in the Tropical Indian Ocean, Part I: The Role of Remote Forcing from Tropical Pacific, *COLA technical report.*, February 2005, 43 pp.

James, I. N., 1987: Suppression of baroclinic instability in horizontally sheared flows. *J. Atmos. Sci.*, **44**, 3710-3720.

Kiehl J. T., J. J. Hack, G. B. Bonan, B. A. Boville, D. L. Williamson, and P. J. Rasch, 1998: The National Center for Atmospheric Research Community Climate Model: CCM3. *J. Climate*, **11**, 1131–1149.

Kitoh, A., S. Yukimoto, A. Noda, and T. Motoni, 1997: Simulated changes in the Asian summer monsoon at times of increased atmospheric CO2. *J. Meteorol. Soc. Japan*, **75**, 1019-1031.

Kitoh, A., 2007: ENSO modulation by mountain uplift. *Clim. Dyn*., **28**, 781-796.

Klein, S. A., B. J. Soden, and N. C. Lau, 1999: Remote sea surface temperature variations during ENSO: evidence for a tropical atmospheric bridge. *J. Climate*, **12**, 917–932.

Krishnamurthy, V., and B. P. Kirtman, 2003: Variability of the Indian Ocean: Relation to monsoon and ENSO. *Quart. J. Roy. Meteor. Soc*., **129**, 1632-1646.

Kutzbach, J. E., P. J. Guetter, W. F. Ruddiman, and W. L. Prell, 1989: The sensitivity of climate to Late Cenozoic uplift in southern Asia and the American west: Numerical experiments. *J. Geophys. Res.*, **103**, 14451-14510.

Lindzen, R. S., and B. Farrell, 1980: The role of the polar regions in global climate, and a new parameterization of global heat transport. *Mon. Weath. Rev*, **108**, 2064-2079.

Luo H. and M. Yanai, 1992: The large-scale circulation and heat source over the Tibetan Plateau and surrounding areas during the early summer of 1979. Part II: Heat and moisture budgets. *Mon. Weath. Rev*, **112**, 966-989.

Lau, N-C., A. Leetmaa, M. J. Nath, and H-L. Wang, 2005: Influences of ENSO-induced Indo-Western Pacific SST anomalies on extratropical atmospheric variability during the Boreal summer. *J. Climate.*, **18**, 2922-2942.

Lee S., and I. M. Held, 1993: Baroclinic wave packets in models and observations. *J. Atmos. Sci.*, **50**, 1737-1750.

Lee, W.-J., and M. Mak, 1996: The role of orography in the dynamics of storm tracks. *J. Atmos. Sci.*, **53**, 1737-1750.

Lorenz, E. N., 1955: Available potential energy and the maintenance of the general circulation, Tellus, **7**, 157-167.

Nakamura, H., 1992: Midwinter suppression of baroclinic wave activity in the Pacific. *J. Atmos. Sci.*, **49**, 1629-1642.

Nakamura, H., and T. Sampe 2002: Trapping of synoptic-scale disburbances into the North-Pacific subtropical jet core in midwinter. *Geophys. Res. Lett.*, **29**, No. 16, 10.1090/2002GL015535.

Murgugudde, R., and A. J. Busalacchi, 1999: Interannual variability of the dynamics and thermodynamics of the tropical Indian Ocean. *J. Climate.*, **12**, 2300-2326.

Orlansky, I., and J. Katzfey, 1991: The life cycle of a cyclone wave in the Southern Hemisphere. Part I: Eddy energy budget. *J. Atmos. Sci.*, **48**, 1972-1998.

Orlansky, I., and E. K. M. Chang, 1993: Ageostrophic geopotential fluxes in downstream and upstream development of baroclinic waves. *J. Atmos. Sci.*, **50**, 212-225.

Parthasarathy, B., A.A. Munot, and D.R. Kothawale, 1995: Monthly and seasonal rainfall series for All-India homogeneous regions and meteorological subdivisions:1871-1994. *Contributions from Indian Institute of Tropical Meteorolgy*, Research Report RR-065, Aug. 1995, Pune 411 008 INDIA.

Peixoto, J., and A. Oort, 1992: *Physics of Climate*. American Institute of Physics.

Penny, S., G. H. Roe, and D. S. Battisti, 2009: The source of the midwinter suppression in storminess over the North Pacific. *J. Climate*, **23**, 634-648.

Rayner, N. A.; Parker, D. E.; Horton, E. B.; Folland, C. K.; Alexander, L. V.; Rowell, D. P.; Kent, E. C.; Kaplan, A. (2003) Global analyses of sea surface temperature, sea ice, and night marine air temperature since the late nineteenth century. *J. Geophys. Res*, **108**, D14, 4407 10.1029/2002JD002670

Reynolds, R. W., N. A. Rayner, T. M. Smith, D. C. Stokes, and W. Wang, 2002: An improved in situ and satellite SST analysis for climate. *J. Climate*, **15**, 1609–1625.

Robinson, D. P., R. B. Black, and B. A. McDaniel, 2006: A Siberian precursor to midwinter intraseasonal variability in the North Pacific storm track. *Geophys. Res. Lett.*, **33**, L15811, doi: 10.1029/2006GL026458.

Rodwell, M. J. and B. J. Hoskins, 1996: Monsoons and the dynamics of desert. *Quart. J. Roy. Meteor. Soc*., **122**, 1385-1404.

Rodwell, M. J. and B. J. Hoskins, 2001: Subtropical anticyclones and summer monsoons. *J. Climate*, **14**, 3192–3211.

Shaw, T. A., M. Sigmond, T. G. Shepherd and J. F. Scinocca, 2009: Sensitivity of simulated climate to conservation of momentum in gravity wave drag parameterization. *J. Climate*, **22**, 2726-2742.

Shukla, J., Predictability of the tropical atmosphere, the tropical oceans and TOGA, In *Proceedings of the International Conference on the Tropical Ocean Global Atmosphere (TOGA) Programme*, Vol. 2., WCRP-91, pp. 725-730, World Climate Research Programme, Geneva, Switzerland, 1995.

Shukla, 2007: Monsoon mysteries. *Science.*, **318**, 204-205.

Simmons, A. J., and B. J. Hoskins, 1979: The downstream and upstream development of unstable baroclinic waves. *J. Atmos. Sci.*, **36,** 1239–1254.

Son, S.-W., S. Lee, S. B. Feldstein, and J. E. Ten Hoeve, 2008: Time scale and feedback of zonal mea flow variability. *J. Atmos. Sci.*, **65**, 935-952.

Son, S.-W., M. Ting, and L. M. Polvani, 2009: The effect of topography on storm track intensity in a relatively simple general circulation model. *J. Atmos. Sci.*, **66**, 393-411.

Stowasser, M., H. Annamalai, and J. Hafner, 2009: Response of the South Asian Summer Monsoon to Global Warming: Mean and Synoptic Systems. *J. Climate* (**in press**)

Su, H., J. D. Neelin, and C. Chou, 2001: Tropical teleconnection and local response to SST anomalies during the 1997-8 El Nino. *J. Geophys. Res.*, **106**, 20,025-20,043.

Ting, M., 1994: Maintenance of northern summer stationary waves in a GCM. *J. Atmos. Sci.*, **51**, 3286-3308.

Terray, P., P. Delecluse, S. Labattu and L. Terray, 2003: Sea surface temperature associations with the late Indian summer monsoon, *Clim. Dyn*., **21**, 593-618.

Uppala, S. M., et al., 2005: The ERA-40 re-analysis, *Q. J. R. Meteorol. Soc.*, **131**, 2961–3012.

Vallis, G. K. and Gerber, E. P. 2008: Local and Hemispheric Dynamics of the North Atlantic Oscillation, Annular Patterns and the Zonal Index. *Dyn. Atmos. Oceans*, **44**, 184-212.

Watanabe, M., and F.F. Jin, 2003: A moist linear baroclinic model: Coupled dynamical-convective response to El Nino. *J. Climate.*, **16**, 1121-1139.

Webster, P. J., et al, 1998: Monsoons - Processes, predictability, and the prospects for prediction. *J. Geophys. Res.*, **103**, 14451-14510.

Webster, P. J., A. M. Moore, J. P. Loschnigg, and R. R. Leben, 1999: Coupled oceanic-atmospheric dynamics in the Indian Ocean during 1997-8. *Nature*, **401**, 356-360.

Xie, S.-P., K. Hu, J. Hafner, H. Tokinaga, Y. Du, G. Huang, and T. Sampe, 2009: Indian Ocean capacitor effect on Indo-western Pacific climate during the summer following El Nino. *J. Climate*, **22**, 730-747.

Xie, S.-P., H. Annamalai, F.A. Schott and J.P. McCreary, 2002: Structure and mechanisms of South Indian Ocean climate variability. *J. Climate.*, **15**, 864-878.

Xie, P., and P. A. Arkin, 1997: Global Precipitation: A 17-Year Monthly Analysis Based on Gauge Observations, Satellite Estimates, and Numerical Model Outputs. Bull. Amer. Meteor. Soc., **78**, 2539-2558.

Yanai, M. and G. X. Wu, 2006: Effects of the Tibetan Plateau. *The Asian Monsoon*, edited by B. Wang, pp. 513-549, Berlin: Springer.

Yanai, M., C.-F. Li, and Z. Song, 1992: Seasonal heating of the Tibetan Plateau and its effects on the evolution of the Asian summer monsoon. *J. Meteor. Soc. Japan*, **70**, 319-351.

Yasunari, T., K. Saito, and K. Takata, 2006: Relative role of large-scale orography and land surface processes in the global hydroclimate. Part I: Impacts on monsoon systems and the tropics. *J. Hydrometeor*, **7**, 626-641.

Yu, J.-Y., and D. L. Hartmann, 1995: Orographic influences on the distribution and generation of atmospheric variability in a GCM. *J. Atmos. Sci.*, **52**, 2428-2443.

Zhang, G. J. and N. A. McFarlane, 1995: Role of convective-scale momentum transport in climate simulation. *J. Geophys. Res.*, **100**, 1417-1426.

Zhang, Y. Q. and I. M. Held, 1999: A linear stochastic model of a GCM's midlatitude storm tracks. *J. Atmos. Sci.*, **56**, 3416-3435.

Zhang, G. J. and M. Mu, 2005: Effects of modifications to the Zhang-McFarlane convection parameterization on the simulation of the tropical precipitation in the National Center for Atmospheric Research Community Climate Model, version 3. *J. Geophys. Res.*, **110**, D09109.

Zurita-Gotor, P., and E. K. M. Chang, 2005: The impact of zonal propagation and seeding on the eddy-mean flow equilibrium of a zonally varying two-layer model. *J. Atmos. Sci.*, **62**, 2261-2273